



HAL
open science

Descendants of the first stars: the distinct chemical signature of second-generation stars

Tilman Hartwig, Naoki Yoshida, Mattis Magg, Anna Frebel, Simon C. O. Glover, Facundo A. Gómez, Brendan Griffen, Miho N. Ishigaki, Alexander P. Ji, Ralf S. Klessen, et al.

► To cite this version:

Tilman Hartwig, Naoki Yoshida, Mattis Magg, Anna Frebel, Simon C. O. Glover, et al.. Descendants of the first stars: the distinct chemical signature of second-generation stars. Monthly Notices of the Royal Astronomical Society, 2018, 478, pp.1795-1810. 10.1093/mnras/sty1176 . insu-03747684

HAL Id: insu-03747684

<https://insu.hal.science/insu-03747684>

Submitted on 8 Aug 2022

HAL is a multi-disciplinary open access archive for the deposit and dissemination of scientific research documents, whether they are published or not. The documents may come from teaching and research institutions in France or abroad, or from public or private research centers.

L'archive ouverte pluridisciplinaire **HAL**, est destinée au dépôt et à la diffusion de documents scientifiques de niveau recherche, publiés ou non, émanant des établissements d'enseignement et de recherche français ou étrangers, des laboratoires publics ou privés.

Descendants of the first stars: the distinct chemical signature of second-generation stars

Tilman Hartwig,^{1,2,3,4*} Naoki Yoshida,^{1,2} Mattis Magg,⁵ Anna Frebel,⁶ Simon C. O. Glover,⁵ Facundo A. Gómez,^{7,8} Brendan Griffen,⁶ Miho N. Ishigaki,² Alexander P. Ji,^{9†} Ralf S. Klessen,^{5,10} Brian W. O’Shea^{11,12,13,14} and Nozomu Tominaga^{2,15}

¹Department of Physics, School of Science, University of Tokyo, Bunkyo, Tokyo 113-0033, Japan

²Kavli IPMU (WPI), The University of Tokyo, Kashiwa, Chiba 277-8583, Japan

³Sorbonne Universités, UPMC Univ Paris 06, UMR 7095, Institut d’Astrophysique de Paris, F-75014 Paris, France

⁴CNRS, UMR 7095, Institut d’Astrophysique de Paris, F-75014 Paris, France

⁵Universität Heidelberg, Zentrum für Astronomie, ITA, Albert-Ueberle-Straße 2, D-69120 Heidelberg, Germany

⁶Department of Physics and Kavli Institute for Astrophysics and Space Research, MIT, Cambridge, MA 02139, USA

⁷Instituto de Investigación Multidisciplinar en Ciencia y Tecnología, Universidad de La Serena, Raúl Bitrán 1305, La Serena, Chile

⁸Departamento de Física y Astronomía, Universidad de La Serena, Av. Juan Cisternas 1200 N, La Serena, Chile

⁹The Observatories of the Carnegie Institution of Washington, 813 Santa Barbara St, Pasadena, CA 91101, USA

¹⁰Universität Heidelberg, Interdisziplinäres Zentrum für Wissenschaftliches Rechnen, INF 205, D-69120 Heidelberg, Germany

¹¹Department of Computational Mathematics, Science and Engineering, Michigan State University, MI 48823, USA

¹²Department of Physics and Astronomy, Michigan State University, MI 48823, USA

¹³National Superconducting Cyclotron Laboratory, Michigan State University, MI 48823, USA

¹⁴Joint Institute for Nuclear Astrophysics – Center for the Evolution of the Elements, USA

¹⁵Department of Physics, Faculty of Science and Engineering, Konan University, 8-9-1 Okamoto, Kobe, Hyogo 658-8501, Japan

Accepted 2018 April 25. Received 2018 April 20; in original form 2018 January 13

ABSTRACT

Extremely metal-poor (EMP) stars in the Milky Way (MW) allow us to infer the properties of their progenitors by comparing their chemical composition to the metal yields of the first supernovae. This method is most powerful when applied to mono-enriched stars, i.e. stars that formed from gas that was enriched by only one previous supernova. We present a novel diagnostic to identify this subclass of EMP stars. We model the first generations of star formation semi-analytically, based on dark matter halo merger trees that yield MW-like haloes at the present day. Radiative and chemical feedbacks are included self-consistently and we trace all elements up to zinc. Mono-enriched stars account for only ~ 1 per cent of second-generation stars in our fiducial model and we provide an analytical formula for this probability. We also present a novel analytical diagnostic to identify mono-enriched stars, based on the metal yields of the first supernovae. This new diagnostic allows us to derive our main results independently from the specific assumptions made regarding Pop III star formation, and we apply it to a set of observed EMP stars to demonstrate its strengths and limitations. Our results may provide selection criteria for current and future surveys and therefore contribute to a deeper understanding of EMP stars and their progenitors.

Key words: methods: analytical – stars: abundances – stars: Pop III – (galaxies:) Local Group – (cosmology:) early Universe.

1 INTRODUCTION

The first stars in the Universe (the so-called Pop III stars) are of fundamental importance for understanding galaxy formation. They

enriched the primordial interstellar medium (ISM) and intergalactic medium with heavy elements, they contributed to the reionization of the Universe, and they played a crucial role in the formation of the first supermassive black holes. Owing to the lack of efficient coolants in metal-free gas, we expect the first stars to have a higher characteristic mass than is found for present-day star formation. Direct observations of the first stars to test the theories of their formation are also lacking. Our knowledge about the mass distribu-

† Hubble Fellow.

* E-mail: tilman.hartwig@ipmu.jp

tion of the first stars is thus mainly based on theoretical models and simulations (Glover 2013; Greif 2015). Another independent constraint is the absence of any low-mass Pop III survivors in the Milky Way (MW), which limits the masses of the first stars to $\gtrsim 0.8 M_{\odot}$ (Bond 1981; Hartwig et al. 2015; Komiya, Suda & Fujimoto 2016; Ishiyama et al. 2016; Dutta et al. 2017; Magg et al. 2018).

Stellar archaeology provides a powerful approach to constrain the nature and properties of the first stars (Frebel & Norris 2015). Spectroscopic observations of extremely metal-poor (EMP) stars in the MW enable measurements of their chemical composition. The relative abundances of the different elements can then be compared with the theoretically predicted yields of their putative progenitor supernovae (SNe). Several studies have successfully interpreted the abundance signatures of individual EMP stars as the fingerprint of Pop III SNe, and obtained estimates for the stellar mass of the corresponding progenitor (Ishigaki et al. 2014; Keller et al. 2014; Tominaga, Iwamoto & Nomoto 2014; Ji, Frebel & Bromm 2015; Placco et al. 2015, 2016; Chen et al. 2017a; Fraser et al. 2017; Ishigaki et al. 2018). However, a major assumption of this reverse-engineering problem is that the EMP star carries the chemical imprint of only one SN. Accounting for metal contributions from several SNe would require additional free parameters, and consequently weakens the constraints due to degeneracies between the individual yields.

A key challenge of stellar archaeology is therefore to identify mono-enriched second-generation stars, as they are most valuable for constraining the properties of the first stars. Here, we define ‘mono-enriched’ second-generation stars as stars that formed from gas that was enriched by exactly one Pop III SN. In contrast, we refer to stars that carry the combined chemical signature of more than one SN as ‘multi-enriched’.

Metallicity alone is not a reliable tracer of the stellar population because the metallicity of gas enriched by a single Pop III SN depends sensitively on the metal yield of the SN, which varies greatly, particularly for an element such as Fe, and on the degree of metal mixing, which is poorly constrained. For example, in our models, we find mono-enriched second-generation stars with metallicities¹ $[\text{Fe}/\text{H}] > -3$ and later generations of star formation with metallicities as small as $[\text{Fe}/\text{H}] \sim -3$. The carbon-enhancement of most EMP stars has been claimed as an additional signature of second-generation stars, emerging from faint Pop III SNe (Beers, Preston & Shectman 1992; Aoki et al. 2007; Ishigaki et al. 2014; Skúladóttir et al. 2015). In this paper, we investigate further indicators and diagnostic to successfully identify mono-enriched second-generation stars, based on their chemical abundance. This allows us to construct samples of stars that are mono-enriched based on our current understanding of Pop III SNe.

Special subclasses of second-generation stars are those that form from gas that was enriched by a pair-instability supernova (PISN). These very energetic explosions of massive metal-poor stars are the final fates of non-rotating Pop III stars in the mass range 140–260 M_{\odot} (Barkat, Rakavy & Sack 1967; Rakavy & Shaviv 1967; Fraley 1968; Bond, Arnett & Carr 1984; Fryer, Woosley & Heger 2001). They eject more metals than core collapse SNe and can therefore enrich the ISM of their host halo to higher metallicities, beyond $[\text{Fe}/\text{H}] \sim -3$. This makes it more difficult to search for second-generation stars that form from the debris of a PISN because

the number of ordinary stars increases with metallicity and the fraction of PISN-enriched stars at $[\text{Fe}/\text{H}] > -3$ is very small (de Bannassuti et al. 2017). The nucleosynthetic yield of a PISN has a strong deficiency of the odd-charged elements (Heger & Woosley 2002), but this signature has not yet been conclusively observed in stellar archaeology surveys (Aoki et al. 2014). It is therefore crucial to derive the distinct chemical signature of second-generation stars that form from gas enriched by a PISN. In this paper, we provide guidance to identify mono-enriched stars from core collapse or pair-instability SNe and also derive the completeness fraction of current stellar archaeology surveys that focus on $[\text{Fe}/\text{H}] < -3$.

2 METHODOLOGY

2.1 Semi-analytical model of star formation

Cosmic structure formation proceeds hierarchically from small matter overdensities in the early Universe via accretion and mergers. Hierarchical structure formation is dominated by dark matter, which accounts for most of the matter in the Universe. To model the baryonic physics of star and galaxy formation, we can therefore decouple the formation and mergers of dark matter haloes and the physics and stellar feedback within them.

Our semi-analytical approach is based on dark matter merger trees that were separately generated from high-resolution N -body simulations. On top of this dark matter framework, we model star formation and the corresponding feedback self-consistently with a set of analytical recipes. For this study, we use 30 MW-like merger trees from the Caterpillar project (Griffen et al. 2016), which assumes the current dark energy plus cold dark matter (Λ CDM) paradigm with cosmological parameters from (Planck Collaboration XVI 2014). The haloes were selected based on three criteria to resemble the MW: virial masses in the range $0.7 \times 10^{12} < M_{\text{vir}}/M_{\odot} < 3 \times 10^{12}$, no other haloes with $M_{\text{vir}} > 7 \times 10^{13} M_{\odot}$ within 7 Mpc, and no haloes with $M_{\text{vir}} > 0.5 M_{\text{host}}$ within 2.8 Mpc. The mass of a dark matter particle in the highest resolution zoom region is $3 \times 10^4 M_{\odot}$, which is sufficient to resolve also the smallest Pop III star-forming haloes at high redshift (Griffen et al. 2018; Magg et al. 2018). The time between snapshots at high redshift is ~ 5 Myr at $z > 6$ and ~ 50 Myr at $z < 6$. This guarantees a high temporal resolution to model accurately the radiative and chemical feedback of Pop III stars. Our semi-analytical model of Pop III star formation is based on Hartwig et al. (2015) with improvements by Magg et al. (2016, 2018). For further details on the model and a resolution study see Magg et al. (2018).

In the early Universe the main components of primordial gas clouds are hydrogen and helium with H_2 being the most efficient coolant under the conditions considered here. Once a pristine halo reaches the critical mass

$$M_{\text{crit}} = 3.3 \times 10^6 M_{\odot} \left(\frac{1+z}{10} \right)^{-3/2}, \quad (1)$$

cooling by molecular hydrogen is efficient enough to allow the gas to collapse to protostellar densities and trigger star formation (Yoshida et al. 2003; Hummel et al. 2012). Massive stars forming in these haloes produce large numbers of soft ultraviolet photons in the Lyman and Werner bands of H_2 . These Lyman–Werner (LW) photons can readily escape from low-mass haloes (Schauer et al. 2015) and so the onset of Pop III star formation is quickly followed by the growth of an extragalactic LW background. We model the effect of this LW feedback as a uniform background that increases

¹Defined as $[A/B] = \log_{10}(m_A/m_B) - \log_{10}(m_{A,\odot}/m_{B,\odot})$, where m_A and m_B are the abundances of elements A and B and $m_{A,\odot}$ and $m_{B,\odot}$ are the solar abundances of these elements (Asplund et al. 2009).

with time according to

$$F_{21}(z) = 4\pi 10^{-(z-10)/5}, \quad (2)$$

where F_{21} has the units $10^{-21} \text{ erg s}^{-1} \text{ cm}^{-2} \text{ Hz}^{-1}$ (Greif & Bromm 2006). Most haloes are illuminated by an LW flux that is within a factor of two of this mean value (Dijkstra et al. 2008), which justifies this approximate treatment. LW photons can photodissociate H_2 and hence destroy the most important coolant in the early Universe and consequently prevent star formation. In addition to the critical mass required for primordial star formation (equation 1), we therefore check that the halo mass is above (O’Shea & Norman 2008)

$$M_{\text{LW}} = 5 \times 10^5 M_{\odot} + 3.5 \times 10^6 M_{\odot} F_{21}^{0.47}. \quad (3)$$

Baryonic streaming velocities might further alter this threshold and require a higher critical mass, but the relative importance of this effect is still debated (Stacy, Bromm & Loeb 2011; Greif et al. 2011a; Naoz, Yoshida & Gnedin 2013; Tanaka & Li 2014; Hirano et al. 2017; Schauer et al. 2017; Schauer et al. in preparation).

Once we identify a halo in which Pop III stars can form, we assign individual metal-free stars to it by sampling stochastically from a logarithmically flat initial mass function (IMF) until the total stellar mass is above

$$M_* = \eta_{\text{III}} \frac{\Omega_b}{\Omega_m} M_h, \quad (4)$$

where η_{III} is the star formation efficiency (SFE) of Pop III stars and M_h is the mass of the halo. The SFE and the lower and upper limit of the Pop III IMF are calibrated to match observational constraints (see Section 3.1). We assume that star formation is instantaneous and model the ionizing feedback on subsequent star formation. The emerging H II regions around star-forming haloes suppress star formation in their vicinity by photoionization heating and we allow star formation in haloes that are within the H II region of a neighbouring halo only if $T_{\text{vir}} > 10^4 \text{ K}$.

Once a star explodes as an SN, we follow the expansion of its metal-enriched shell. For Pop III SNe, we assume a constant velocity of 10 km s^{-1} in the intergalactic medium (Smith et al. 2015) and for metals from SNe of later generation stars we model their expansion as a momentum-driven snowplough (see Magg et al. 2018 for details on the ionizing feedback and external enrichment).

When a halo has been enriched with metals, the second-generation stars form from this enriched interstellar medium (e.g. Chiaki, Yoshida & Hirano 2016). We distinguish two different enrichment channels: if the haloes has been enriched internally by Pop III stars in the same halo, we delay the formation of second-generation stars by the recovery time $t_{\text{recov}} = 100 \text{ Myr}$ (Greif et al. 2010; Whalen et al. 2013; Jeon et al. 2014; Smith et al. 2015; Jeon, Besla & Bromm 2017; Chiaki, Susa & Hirano 2018). If a previously pristine halo is externally enriched and has a mass above M_{LW} , Pop II star formation occurs one freefall time after this enrichment with

$$t_{\text{ff}} = 72 \text{ Myr} \left(\frac{1+z}{10} \right)^{-3/2}, \quad (5)$$

where we assume an overdensity of 200 times the mean cosmic density. In this paper, we refer to second-generation stars as those that form after the first metal enrichment of a halo. Due to the delay between the first enrichment and the onset of second-generation star formation, the host galaxy can be enriched by multiple enrichment events or merge with an already enriched galaxy before the second-generation stars forms.

The main topics of this paper are the nature, chemical characteristics, and unique signature of second-generation stars. We assume

that the composition of such a second-generation star is defined at the moment of its formation and does not change during the lifetime due to possible pollution by ISM accretion (Tanaka et al. 2017, see also Yoshii 1981; Frebel, Johnson & Bromm 2009; Komiya et al. 2010; Hattori et al. 2014; Johnson 2015; Komiya, Suda & Fujimoto 2015; Shen et al. 2017). Whenever we refer to the chemical composition of second-generation stars, we implicitly refer to the chemical composition of the ISM from which these second-generation stars form.

2.2 SN yields and chemical enrichment

One novel feature of our semi-analytical model is the tracking of chemical elements up to zinc. This enables us to calibrate our model based on various observations and we obtain crucial insight into the chemical enrichment history of the MW. In this section, we briefly summarize the main features of our model of chemical evolution.

For Pop III stars, we use the tabulated metal yields as a function of progenitor mass by Nomoto, Kobayashi & Tominaga (2013). The theoretical uncertainty for the metal yields between different models (Heger & Woosley 2010; Limongi & Chieffi 2012) is of the order 0.3 dex for carbon to zinc, as we will discuss below. Independent of the SN progenitor mass, we assume that 20 per cent of the ejected metals fall back within the recovery time and 80 per cent are ejected from the gravitational potential of the halo (Wise & Abel 2008; Ritter et al. 2012). For internal and external enrichment, we assume instantaneous mixing and if more than one SN contributes to the enrichment, the individual metal yields are added. To model inhomogeneous mixing of the metals with the ISM, we assume that only a fraction f_{dil} of all hydrogen in the halo mixes with the metals. This approach is consistent with more advanced theoretical models (Starkenburger et al. 2013; Chen et al. 2017a; Hirai & Saitoh 2017; Sarmiento, Scannapieco & Pan 2017; Sarmiento et al. 2018) and we draw the dilution factors from a lognormal distribution with mean $\mu = 10^{-1.5}$ and width $\sigma = 0.75$ dex. More realistic hydrodynamical simulations of the mixing of the first SN yields have been performed self-consistently in 3D by other groups (Greif et al. 2007; Whalen et al. 2008; Wise & Abel 2008; Greif et al. 2010; Ritter et al. 2012; Vasiliev et al. 2012; Wise et al. 2012; Jeon et al. 2014; Safranek-Shrader, Milosavljević & Bromm 2014; O’Shea et al. 2015; Ritter et al. 2015, 2016; Smith et al. 2015; Chen et al. 2017b; Sharma et al. 2018).

We do not account for metal enrichment by Type Ia SNe or red giant branch stars because these processes are expected to occur at later cosmic times and do not significantly contribute to the enrichment of second-generation stars (Komiya & Shigezama 2016).

To model the metal yields from Pop II stars, we assume that 5 per cent of the stellar mass is eventually ejected as metals (Vincenzo et al. 2016). Since we are interested in the first enrichment events, we presume for simplicity that all of these metals are ejected by Type II SNe. To determine how this mass of metals is distributed over the individual elements, we apply the distribution of chemical yields by Nomoto et al. (2013) for stars at $Z = 0.001$ and average the contribution by SNe with different progenitor masses over a Salpeter IMF in the range $10\text{--}40 M_{\odot}$.

One important observed characteristic of EMP stars is their frequently high carbon-to-iron ratio, which we aim to reproduce in our model by including faint SNe. We illustrate the $[\text{C}/\text{Fe}]$ ratio as a function of Pop III progenitor mass in Fig. 1 for different types of SNe.

A faint SN refers to an explosion with a very small ejected ^{56}Ni mass either due to a low explosion energy (Chen et al. 2017a) or

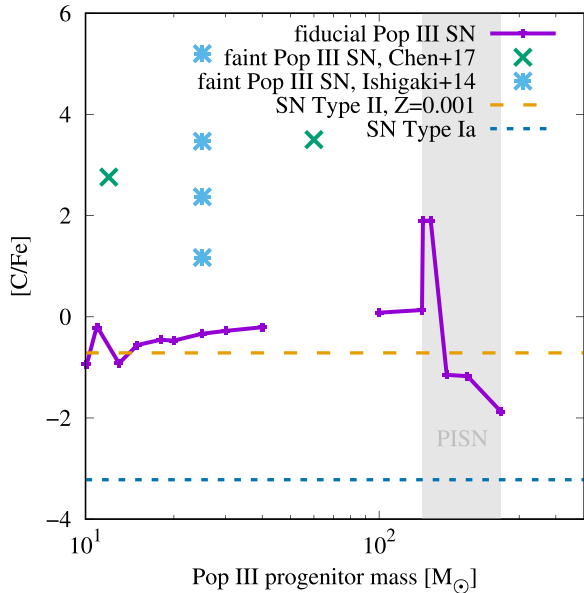


Figure 1. Carbon-to-iron ratio, $[C/Fe]$, as a function of the Pop III SN progenitor mass (solid, Nomoto et al. 2013). For comparison, we also show the yields of Type Ia (short-dashed, Seitzzahl et al. 2013) and Type II SNe (long-dashed, Nomoto et al. 2013). The yields for individual faint SNe are based on Chen et al. (2017a) and Ishigaki et al. (2014). Pair-instability supernovae (PISNe) with a progenitor mass of $\sim 150 M_{\odot}$ yield a very high $[C/Fe]$ (because they eject relatively little iron), but PISNe with a progenitor mass of $\sim 250 M_{\odot}$ yield a very low, even significantly subsolar value of $[C/Fe]$. The explosion energies of Type II SNe are assumed to be 10^{51} erg. Faint SNe with lower explosion energies have generally higher $[C/Fe]$ because more iron falls back on to the compact remnant.

large-scale mixing and fallback in aspherical explosions (Tominaga, Umeda & Nomoto 2007). To account for faint SNe, we include the corresponding yields by Ishigaki et al. (2014) in our model and discuss the calibration of the fraction of faint SNe in Section 3.1. These models are all for faint SNe with a progenitor mass of $25 M_{\odot}$, but can be taken as representative for faint SNe occurring in the mass range of $10\text{--}40 M_{\odot}$.

3 RESULTS

3.1 Calibration

We use the observed fraction of carbon-enhanced metal-poor (CEMP) stars and the distribution of EMP halo stars to calibrate our model. However, our model is not intended to reproduce these functions over a broad metallicity range because we focus on second-generation stars. In general, metal-poor stars can form after any number of previous generations of star formation, but each additional enrichment event results in higher stellar metallicities. Therefore, we focus on the stars with a metallicity of $[Fe/H] \leq -3$ for calibration purposes because we can assume that Pop III stars dominate the enrichment of these EMP stars. The fraction of CEMP stars might be an inherent signature of the metal yields of Pop III stars (Frebel et al. 2007; Cooke et al. 2011; Lee et al. 2013; Norris et al. 2013; Cooke & Madau 2014; Placco et al. 2014; Bonifacio et al. 2015; Maeder, Meynet & Chiappini 2015; Caffau et al. 2016; Jeon, Besla & Bromm 2017), and thus less affected by any missing contribution from later generations.

Table 1. Parameter values in our fiducial model. This set of parameters best reproduces observations at $[Fe/H] \leq -3$, as we show below.

Parameter	Value
Mass threshold for Pop III	Equation (1)
Mass threshold with LW feedback	Equation (3)
Pop III SFE	$\eta_{\text{III}} = 0.001$
Pop II SFE	$\eta_{\text{II}} = 0.01$
Fraction of faint SNe	$f_{\text{faint}} = 40$ per cent
Metal fallback fraction	$f_{\text{fallback}} = 20$ per cent
Metal ejection fraction	$f_{\text{eject}} = 80$ per cent
Pop III SN wind velocity	$v = 10 \text{ km s}^{-1}$
Lower IMF limit	$M_{\text{min}} = 3 M_{\odot}$
Upper IMF limit	$M_{\text{max}} = 150 M_{\odot}$
Recovery time	$t_{\text{recov}} = 100 \text{ Myr}$
Mean of dilution distribution	$\mu = 10^{-1.5}$
Width of dilution distribution	$\sigma = 0.75 \text{ dex}$

3.1.1 Fiducial model

In this section, we present our fiducial parameters, motivate that they are physically reasonable, and that they meet additional observational constraints. Throughout the paper, we restrict our analysis to the MW and satellites within $R_{\text{vir}} = 300 \text{ kpc}$ from the MW centre at $z = 0$ (if not explicitly stated otherwise).

The main model parameters and their fiducial values are summarized in Table 1. The Pop III SFE is a crucial parameter for stellar archaeology since it defines the gas mass fraction that turns into stars and hence the average number of Pop III SNe per minihalo. As well as calibrating it with stellar archaeology observations, we also enforce two additional constraints. We require that our choice of η_{III} leads to an optical depth for the Thomson scattering of CMB photons, $\tau = 0.069$, consistent with the value measured by Planck Collaboration XIII (2016). See Hartwig et al. (2015) for a more detailed discussion on how the ionization history of the Universe can be used to calibrate the Pop III SFE in semi-analytical models. We also confirm that the mass in Pop III stars per minihalo implied by our adopted SFE is consistent with the values found in detailed hydrodynamical simulations of Pop III star formation. For example, for a minihalo with a total mass of $3 \times 10^6 M_{\odot}$ (the lowest mass minihalo capable of forming Pop III stars at redshift $z \sim 20$), our fiducial Pop III SFE predicts a total Pop III stellar mass of around $500 M_{\odot}$, in good agreement with the values of order $100\text{--}1000 M_{\odot}$ found in numerical simulations (Hirano et al. 2014; Susa, Hasegawa & Tominaga 2014). These numerical results can be seen as a lower limit because most simulations focus on the first high redshift peaks but we also expect metal-free star formation at $z < 10$ in more massive haloes. The fractions of ejected metals and metals that fall back on to the halo after an SN are consistent with the results of Ritter et al. (2012).

We show in Fig. 2 that we can reproduce the metallicity distribution function (MDF) and the fraction of CEMP-no stars as a function of metallicity with this set of parameters. CEMP-no stars are a subclass of CEMP stars with $[Ba/Fe] \leq 0.0$, i.e. with no enhancement in neutron capture elements. We limit this comparison to stars with $[Fe/H] \leq -3$ because above this value we expect contributions from later generations of stars to become important that we do not model self-consistently. In the low metallicity range, we can successfully reproduce both observed distributions with our model. We used the fraction of CEMP-no stars with $[C/Fe] > 0.7$ from Placco et al. (2014) and the MDF from Yong et al. (2013) for comparison, since the latter is more recent and complete than the MDF provided by

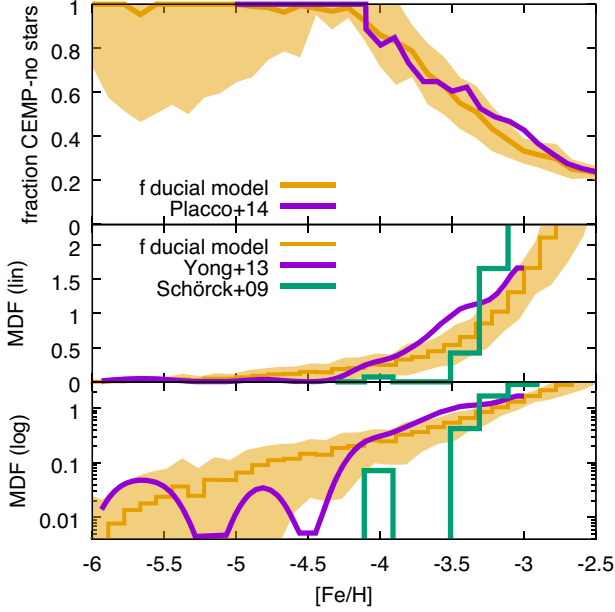


Figure 2. Top: Fraction of CEMP-no stars ($[C/Fe] > 0.7$) as a function of $[Fe/H]$ predicted by our model (orange) with the observed distribution (purple, Placco et al. 2014) shown for comparison. Below: Predicted (orange) and observed (green, Schörck et al. 2009; purple, Yong et al. 2013) MDFs, normalized to the number of stars below $[Fe/H] \leq -3$ in linear (middle) and logarithmic (bottom) scaling. The shaded regions indicate the scatter over 30 different merger tree realizations. Our model agrees with the observed distributions from Placco et al. (2014) and Yong et al. (2013) within the statistical uncertainty.

Schörck et al. (2009). Since we average 30 MW-like merger trees, we do not reproduce the sparse sampling at $[Fe/H] \leq -4.5$, but discuss this effect separately below.

Another important and poorly constrained parameter is the fraction of faint SNe, which is assumed to have a direct influence on the fraction of CEMP stars due to the high $[C/Fe]$ yields of this type of SN. We find a best matching value of $f_{\text{faint}} = 40$ per cent. Slightly higher values (Ji et al. 2015; de Bressan et al. 2017) are also compatible within our error margins. The fraction of CEMP stars is mainly controlled by the adopted model for mixing with the ISM and f_{faint} .

3.1.2 Exploring input parameters

We now compare how different parameters affect the results and demonstrate quantitatively that our fiducial set of parameters best reproduces the MDF and the fraction of CEMP-no stars (Fig. 3). If we assume $\mu = 10^{-0.5}$, i.e. that metals ejected by SNe mix with almost all available hydrogen in a halo, we predict too few CEMP-no stars. If we assume that the distribution of dilution factors is too narrow ($\sigma = 0.2$ dex), we predict too many CEMP-no stars with $[Fe/H] \approx -3$. The green line in this plot also demonstrates that our model for a single MW-like merger tree correctly reproduces the sparsely sampled region at $[Fe/H] \leq -4.5$.

To quantify the quality of our calibration and to compare the relative influence of the model parameters in Table 1, we apply the Kolmogorov–Smirnov (KS) test and calculate the maximum difference between the cumulative distribution functions of the two

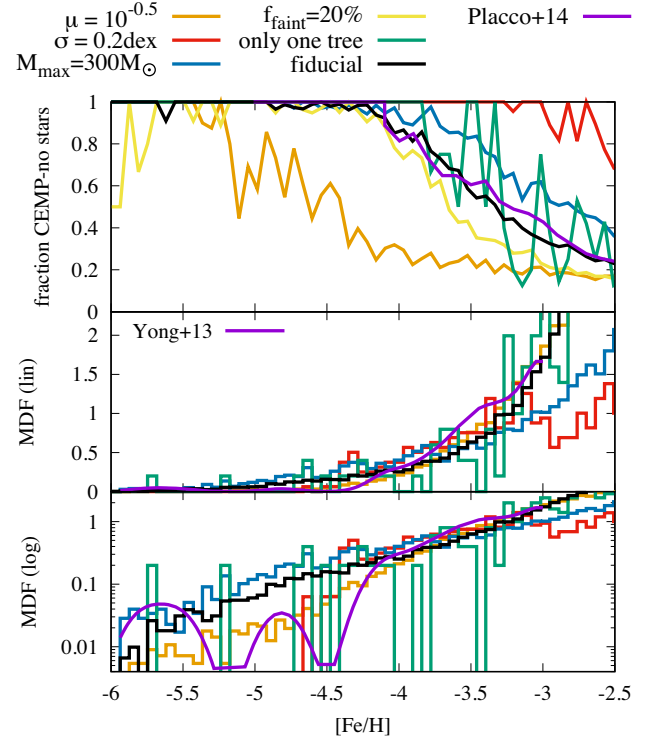


Figure 3. Same as Fig. 2, but showing the effect of varying the model parameters specified in the legend. The results of our fiducial model are shown in black. We also show the results from a realization based on only one tree (green), which highlights the expected stochasticity of the distribution at low $[Fe/H]$. We note that the yellow line in the middle and lower panels ($f_{\text{faint}} = 20$ per cent) is identical with that in the fiducial model.

Table 2. Parameter study and KS-test values (equation 6). Our fiducial model yields the smallest maximum differences between the cumulative distributions of the observations and our model. However, the only model that can be rejected based on this two-sample KS test at the 95 per cent level is the one with $M_{\text{max}} = 300 M_{\odot}$ (see the text).

Parameter	D_{MDF}	D_{CEMP}	Σ
Fiducial	0.08	0.07	0.15
$M_{\text{min}} = 10 M_{\odot}$	0.09	0.11	0.20
$M_{\text{max}} = 120 M_{\odot}$	0.13	0.11	0.24
$M_{\text{max}} = 300 M_{\odot}$	0.24	0.07	0.31
$\eta_{\text{III}} = 0.0005$	0.14	0.05	0.19
$\eta_{\text{III}} = 0.002$	0.12	0.10	0.22
$\eta_{\text{II}} = 0.02$	0.12	0.06	0.18
$t_{\text{recov}} = 10$ Myr	0.13	0.05	0.18
$f_{\text{faint}} = 0.2$	0.08	0.12	0.20
$f_{\text{faint}} = 0.6$	0.08	0.08	0.16
IMF slope: -1	0.14	0.18	0.32
$f_{\text{eject}} = 0.5$	0.14	0.07	0.21
$\mu = 10^{-0.5}$	0.07	0.15	0.22
$\mu = 10^{-2.0}$	0.09	0.07	0.16
$\sigma = 0.2$ dex	0.16	0.16	0.32

observed distributions and our model:

$$D = \max_{x \leq -3} |F_{\text{obs}}(x) - F_{\text{model}}(x)|, \quad (6)$$

where $F(x)$ is the cumulative distribution function and $x = [Fe/H]$. The resulting values for various models are summarized in Table 2. Our fiducial set of parameters minimizes the sum of D_{MDF} and

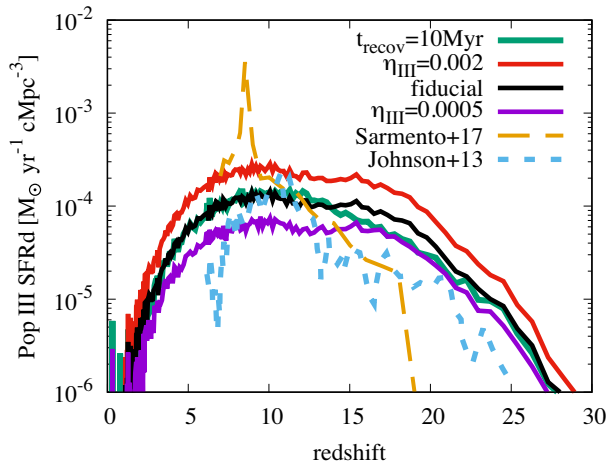


Figure 4. Comparison of the SFRd for Pop III stars as a function of redshift of our model (solid) to the rates by Johnson et al. (2013) and Sarmiento et al. (2017) (dashed). The SFRd scales roughly with the SFE, and in our fiducial model, we find a peak value of $\sim 10^{-4} M_{\odot} \text{ yr}^{-1} \text{ cMpc}^{-3}$ (comoving Mpc) around $z \approx 10$. A shorter recovery time leads to a more efficient suppression of Pop III SF at $z \gtrsim 15$ because Pop II stars can form earlier. The SFRd of our model is averaged over 30 MW-like trees.

D_{CEMP} . To reject the null-hypothesis that our model reproduces the observations at 95 per cent significance level, we determine the corresponding critical distance to be $D_{\text{crit, MDF}} = 0.23$ for the MDF and $D_{\text{crit, CEMP}} = 0.29$ for the fraction of CEMP-no stars. The only parameter choice that can be excluded based on this analysis is $M_{\text{max}} \geq 300 M_{\odot}$ as an upper limit for the Pop III IMF. Since we do not fully explore our 11D parameter space, we can only conclude that our fiducial parameters represent a local optimum, while other parameter combinations may yield a similar or even better fit to the observations. Unfortunately, this also illustrates the weak predictive power of this approach and we do not claim to constrain any of the parameters by fitting a model with 11 free parameters to two observables. A full parameter space exploration could be performed by means of, e.g., Gaussian processes model emulators (e.g. Bower et al. 2010; Gómez et al. 2012, 2014). Nonetheless, our set of initial parameters agrees with other studies and reproduces the main observations provided by stellar archaeology. Moreover, we will show later that our main conclusions can also be derived independently of the specific cosmological model adopted.

We also show the parameter dependence of the Pop III star formation rate density (SFRd) in Fig. 4. It is calculated within the comoving volume of the MW and therefore represents a cosmic overdensity. Our star formation rates are consistent with those in Johnson, Dalla Vecchia & Khochfar (2013), with the upper limit advocated by Visbal, Haiman & Bryan (2015), and with the Thomson scattering optical depth measured by Planck Collaboration XIII (2016). Our results differ from Sarmiento et al. (2017) because they allow Pop III star formation in slightly enriched haloes up to a metallicity of $Z_{\text{crit}} = 10^{-5} Z_{\odot}$, which permits more Pop III star-forming haloes at $z < 10$.

3.2 Internal versus external enrichment

The difference between internal and external enrichment is important because the time-scales of the subsequent collapse and the overall enriching mass depend on the nature of the enrichment. As internal enrichment, we label the inevitable chemical enrichment of

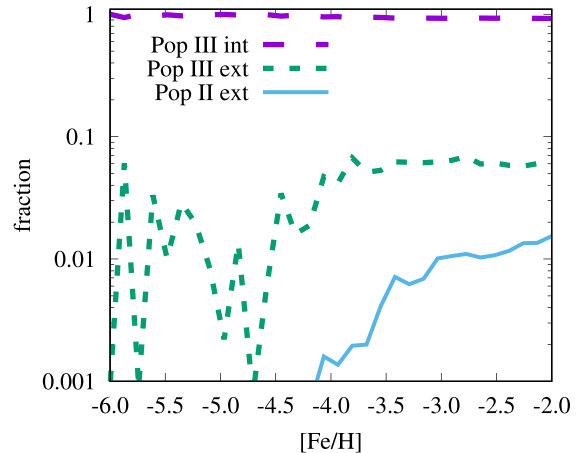


Figure 5. Relative contribution to the metal enrichment of second-generation stars via different enrichment channels (metal mass weighted). The three contributions sum up to 100 per cent. Internal enrichment by Pop III stars dominates at all metallicities and external enrichment by Pop III stars accounts for ~ 10 per cent of the enriching metals above $[\text{Fe}/\text{H}] = -4$. External enrichment by Pop II stars is always sub-dominant ($\lesssim 1$ per cent) for the overall metal budget of second-generation stars.

a halo after star formation. External enrichment occurs when the radius of a metal-enriched bubble is larger than the separation between the centres of two haloes (see Section 2.2), typically of the order 0.1–10 kpc. Both of these enriching events are passed through the merger tree so that a halo at $z = 0$ could have experienced several internal and external enrichment events during its assembly history. We investigate the relative contributions of internal versus external enrichment in Fig. 5.

Internal enrichment is dominant compared to external enrichment prior to the formation of second-generation stars, as has also been shown by Griffen et al. (2018), Visbal, Haiman & Bryan (2018), and Jeon et al. (2017). If haloes are close enough for external enrichment, ionizing feedback is usually also strong enough to suppress star formation, thereby preventing the formation of externally enriched second-generation stars. For this reason, varying the recovery time makes little difference to the external enrichment fractions. The metal contributions in Fig. 5 are averaged and there are individual haloes that are only enriched externally by Pop III or II stars, although their occurrence in number is small. We find that the outcome of second-generation star formation does not strongly depend on environmental effects, such as the clustering of haloes. We also confirm in our semi-analytical model that the radial distribution of haloes hosting second-generation stars follows the radial distributions of all haloes in the local volume at $z = 0$.

In Fig. 6, we see the 3D distribution of haloes in the Local Group at $z = 0$ for one exemplary MW-like merger tree. We find ~ 400 satellites with stellar masses above $1000 M_{\odot}$. The observed number of MW satellites is around 50 (Drlica-Wagner et al. 2015), which seems to be in contradiction with our model and other DM simulations (the ‘missing satellite problem’, see Kauffmann, White & Guiderdoni 1993; Klypin et al. 1999; Moore et al. 1999). However, this discrepancy can be solved by correcting for the completeness bias of the surveys (Kim, Peter & Hargis 2017). We assign stellar masses at $z = 0$ via abundance matching based on the peak mass of each satellite during its assembly history (Garrison-Kimmel et al. 2014). Note that stellar masses below $\sim 5 \times 10^5 M_{\odot}$ should be considered as an extrapolation due to the incompleteness of their observations for low-mass satellites. Moreover, the scatter in the

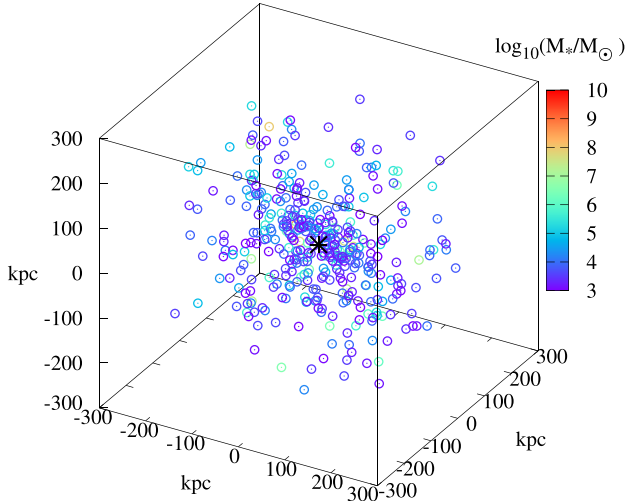


Figure 6. Projection of all star-hosting haloes at $z = 0$ within 300 kpc of the MW main halo for one merger tree realization. The main halo is indicated by the black asterisk and the satellites are colour-coded by their stellar mass.

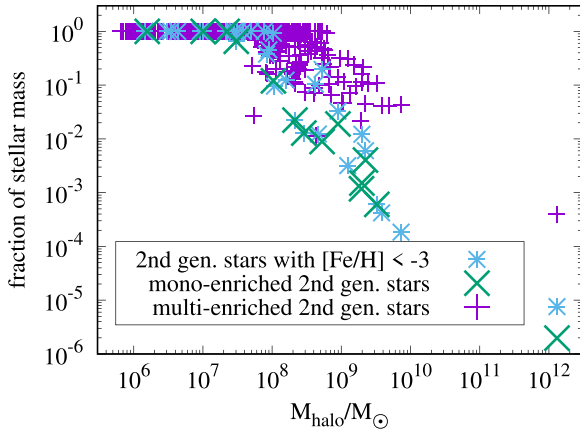


Figure 7. Fraction of all (purple), metal-poor ($[\text{Fe}/\text{H}] < -3$, blue), and mono-enriched (green) second-generation stars relative to the total stellar mass at $z = 0$. Second-generation stars end up in satellites of all masses, but their fraction is much higher in low-mass haloes.

relation between stellar and halo mass becomes more important at lower masses (Garrison-Kimmel et al. 2017). Hydrodynamic simulations indicate that extrapolations to low masses are reasonable (Munshi et al. 2017; Jeon et al. 2017), but our stellar masses at $z = 0$ should be considered as rough estimate for lower-mass satellites.

For a direct comparison of the fractions of second-generation stars, we assume for the mass of the stellar population of the second generation an instantaneous starburst that converts 1 per cent of the gas mass into stars. The resulting fractions as a function of the stellar mass can be seen in Fig. 7. During the assembly of the MW and its satellites, haloes that host second-generation stars merge into larger systems and at $z = 0$ second-generation stars can be found in satellites of all masses. However, the relative contribution of second-generation stars to the total stellar population depends on the host mass, with less massive haloes being more likely to host a higher fraction of second-generation stars. The MW at $z = 0$ consists of e.g. $\lesssim 0.1$ per cent second-generation stars, but only $\sim 10^{-5}$ of all MW stars are metal-poor ($[\text{Fe}/\text{H}] < -3$) and $\sim 10^{-6}$ are mono-enriched second-generation stars. Our analysis shows that the stellar

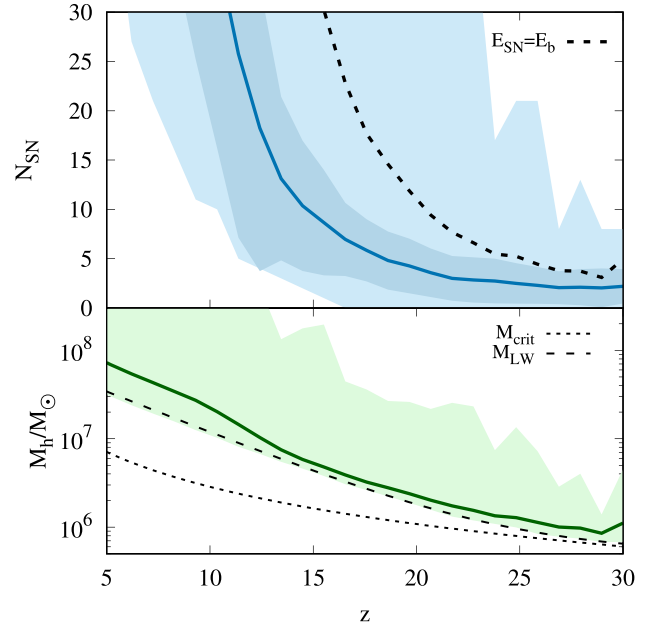


Figure 8. Top: Number of Pop III SNe per minihalo as a function of redshift. Bottom: Halo masses at the moment of Pop III star formation. The solid line indicates the mean, the dark contours the 1σ standard deviation, and the light contours the minimum and maximum values in this redshift bin. The increase of the number of SNe with decreasing redshift is related to the simultaneous increase of the stellar mass that is available per Pop III star-forming halo. In some rare cases at $z > 15$, there are minihaloes with only one SN, but generally, we expect between 5 and 20 SNe per minihalo. The dotted and dashed lines in the bottom panel illustrate the critical masses for Pop III star formation. The dotted line in the top panel indicates the number of SNe required to expel all of the gas from the halo. Haloes with more than this number of SNe may be completely disrupted by Pop III SNe and hence may not form second-generation stars.

population in satellites with $M_h \gtrsim 10^8 M_\odot$ originates dominantly from the second-generation star formation. Although our model predicts a fraction of close to 100 per cent in this mass range, the actual fraction may be lower due to the scatter in the halo to stellar mass relation, which we do not take into account.

These results are in agreement with previous models that show that ultra-faint dwarf galaxies host ancient stellar populations and probe early cosmic star formation (Bullock, Kravtsov & Weinberg 2000; Salvadori & Ferrara 2009; Gao et al. 2010; Starkenburg et al. 2013; Weisz et al. 2014; Ji et al. 2016; Jeon, Besla & Bromm 2017; Starkenburg et al. 2017a; Griffen et al. 2018). This is because ultra-faint dwarf galaxies with $M_h < 2 \times 10^9 M_\odot$ formed $\gtrsim 90$ per cent of their stellar mass prior to reionization (Jeon et al. 2017) and have an average iron abundance of $[\text{Fe}/\text{H}] < -2$ (Kirby et al. 2008).

3.3 Number of Pop III SNe per halo

The chemical signature of second-generation stars can be used to deduce the masses of their Pop III progenitors. For this purpose, we are especially interested in those cases where the ISM was enriched by exactly one previous Pop III SN. However, in most minihaloes, we form Pop III stars in small multiples (Turk, Abel & O’Shea 2009; Stacy, Greif & Bromm 2010; Clark et al. 2011; Greif et al. 2011b; Smith et al. 2011; Susa et al. 2014; Hirano & Bromm 2017), and in Fig. 8, we show the average number of SNe per minihalo. It is an increasing function with decreasing redshift

due to the increasing threshold mass for Pop III star formation. At $z \gtrsim 15$, we expect fewer than 10 SNe per halo, and in individual cases, there are haloes with just one Pop III SN. These are the cradles for mono-enriched second-generation stars.

Minihaloes at high redshift have shallow potential wells and SNe could unbind all the gas in the halo and hence prevent subsequent star formation. To derive the critical number of SNe required to do this, we assume that an SN has on average an energy of 10^{51} erg and that the halo has a gravitational binding energy (Loeb 2010) of

$$E_b = 2.9 \times 10^{53} \left(\frac{M_h}{10^8 M_\odot} \right)^{5/3} \left(\frac{1+z}{10} \right) \text{ erg.} \quad (7)$$

Not all of the injected SN energy will effectively couple to the gas and contribute to its ejection, as some will instead be radiated away. Also the low-density H II region, which surrounds the first stars at the moment of their SN explosions, and the anisotropy of the ISM, which provides channels of least resistance for the energy to escape, reduce the efficiency of SNe in ejecting gas from the galactic potential well. To account for this effect, we assume that only 10 per cent of the SN energy couples efficiently to the gas (Kitayama & Yoshida 2005; Whalen et al. 2008). This yields the number of SNe per halo that is required to unbind all gas as

$$N_{\text{SN}} = 62 \left(\frac{M_h}{10^7 M_\odot} \right)^{5/3} \left(\frac{1+z}{10} \right). \quad (8)$$

The black dashed line in the upper panel of Fig. 8 indicates that this critical value is above the average number of SNe per halo. Nevertheless, some haloes at every redshift have values of N_{SN} above this critical value, and may therefore form fewer multi-enriched second-generation stars than our model assumes, because of the disruption of these haloes by SN feedback. We note, however, that this is a simplistic order of magnitude estimate, and more realistic models show that gas fallback is also possible after several or more energetic SN explosions in a minihalo (Kitayama & Yoshida 2005; Greif et al. 2010; Ritter et al. 2012; Chiaki et al. 2018). Therefore, we do not include this destructive effect of multiple SNe self-consistently in our model, but highlight possible implications in the discussion section.

It is also interesting to examine whether the time between two SNe is long enough for the gas to recollapse and form mono-enriched second-generation stars before the second SN explodes. In Fig. 9, we show a histogram of the times between the explosion of the first and the second SN in minihaloes. The average time between two SNe is much shorter than our assumed recovery time for second-generation star formation. Consequently, the presence of multiple SNe in one minihalo indicates that most stars that form at the onset of Pop II star formation carry the imprint of several Pop III SNe.

We derive the probability that exactly one SN explodes in a minihalo, based on Poisson statistics. For a given Pop III IMF, we calculate how much stellar mass we need on average to form one SN. The mean number of SNe in a halo with stellar mass M_* is then given by

$$\lambda = \frac{M_*}{M_{\text{1SN}}}, \quad (9)$$

where M_{1SN} is the stellar mass to expect on average one SN. By applying Poisson statistics, we calculate the probability to have k SNe going off in one minihalo:

$$p(k) = \frac{\lambda^k}{k!} e^{-\lambda}. \quad (10)$$

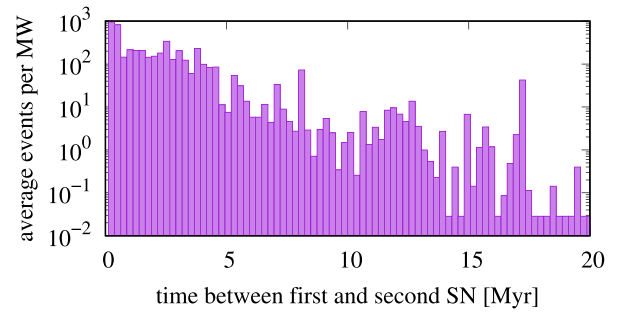


Figure 9. Histogram of the times between the explosion of the first and the second SN in minihaloes per MW-like merger tree. Due to the very short lifetimes of massive stars, the second SN explodes generally within less than 10 Myr after the first one (mind the logarithmic y-axis). This is shorter than the typical recovery time for second-generation star formation (~ 100 Myr). The dominance of short times between SNe illustrates that there is generally not enough time between two SN explosions to form second-generation stars. Instead, they form after most of the Pop III stars in the minihalo have exploded as SNe.

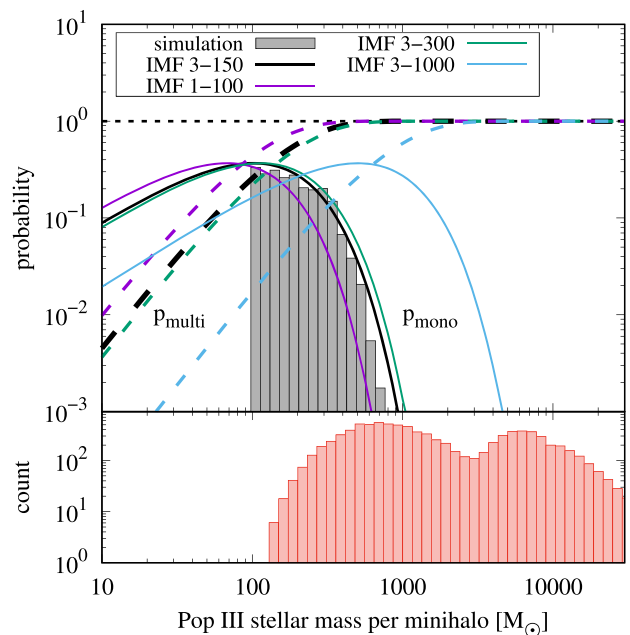


Figure 10. Top: Probability to have exactly one SN (solid) or more than one SN (dashed) per minihalo as a function of the stellar mass for different IMF ranges. The black lines correspond to the analytical prediction of our fiducial model and should be compared to the grey histogram, which is the average over all 30 merger trees. Bottom: histogram of the stellar masses of Pop III star-forming haloes in one MW-like realization. Most Pop III stars form in minihaloes with $M_* \lesssim 1000 M_\odot$ but some form in atomic cooling haloes with stellar masses up to $M_* \gtrsim 10^4 M_\odot$. In these mass ranges, the probability to have exactly one SN in a randomly selected minihalo is < 1 per cent.

The probability to have one SN per halo is given by $p(1)$ and the probability to have more than one SN per halo is given by $1 - p(0) - p(1)$. These probabilities can be seen as a function of the stellar mass in Fig. 10. This analytical derivation is valid as long as the total stellar mass is higher than the upper IMF limit because otherwise the entire IMF cannot be sampled. As we can see in the bottom panel, this criterion is almost always fulfilled in our fiducial model because we form at least $\sim 100 M_\odot$ of Pop III stars per halo

(equation 4). Consequently, the probability to have only one SNe per minihalo is very low, of the order 1 per cent. Instead, we expect second-generation stars to form from gas that has been previously enriched by several SNe. This analytical estimate is very powerful and flexible because it predicts the probability of having more than one SN per minihalo for any possible IMF or stellar mass. The chances to create mono-enriched second-generation stars are highest in the smallest minihaloes because the available gas mass to form stars is lower and hence it is more likely for these haloes to host only one Pop III star that explodes as an SN.

4 CHEMICAL SIGNATURE OF SECOND-GENERATION STARS

We aim to find the optimal diagnostic and selection criteria for EMP stars that are promising mono-enriched candidates, given that only relatively few elements are observable in EMP stars with reasonable effort. We thus need to quantify the likelihood for star-forming gas to have experienced only one prior enrichment event. We first use our semi-analytical model to find which abundances are best suited for this purpose. Then, we present a novel diagnostic that is independent of any model for primordial star formation and only depends on the assumed SN yields.

4.1 Signature based on our cosmological model

In Fig. 11, we display as an example the distribution and probability of finding mono-enriched second-generation stars, calculated for the $[\text{Mg}/\text{C}]$ ratio. The mono-enriched second-generation stars populate specific regimes, different from those of multi-enriched second-generation stars. In general, the probability of mono-enrichment is a decreasing function of metallicity and we find even individual mono-enriched second-generation stars with solar metallicities in our model. The abundance ratio $[\text{Mg}/\text{C}]$ adds an additional constraint with the lowest probability for mono-enrichment around $[\text{Mg}/\text{C}] \sim 0$ and higher probabilities for higher and lower values of $[\text{Mg}/\text{C}]$. Such probability maps can be created for all abundance ratios and in higher dimensions. We limit the discussion to this 2D representation to illustrate the concept since $[\text{Mg}/\text{C}]$ can be observed with little effort and already provides a solid additional constraint.

We also take into account the theoretical uncertainty in the values of the SN yields and the typical observational uncertainties for derived stellar abundances. Ishigaki et al. (2018) compile the observational errors from recent high-resolution spectroscopic studies (Cohen et al. 2013; Yong et al. 2013; Roederer et al. 2014) for the typically observed yields in EMP stars, which are in the range of 0.1–0.5 dex, depending on the element and spectral resolution. Nomoto et al. (2013) compare the predicted metal yields from different groups for Pop III SNe (Tominaga et al. 2007; Heger & Woosley 2010; Limongi & Chieffi 2012) and find a scatter between independent models of on average 0.3 dex for the elements carbon to zinc. We have additionally compared the theoretical yields from Ishigaki et al. (2018) to the predictions from Heger & Woosley (2010) and find a discrepancy for some elements of >1 dex. Although the combined observational and theoretical uncertainty should be evaluated individually for every element, we assume for simplicity 0.5 dex, which is a reasonable average of the various sources of uncertainty. We consequently smooth the abundance-dependent distributions with a Gaussian convolution kernel with the width $\sigma = 0.5$ dex to express that we cannot make exact predictions on finer scales.

We do not account for observational or theoretical uncertainties in the top panel of Fig. 11. This is why the probability map in the

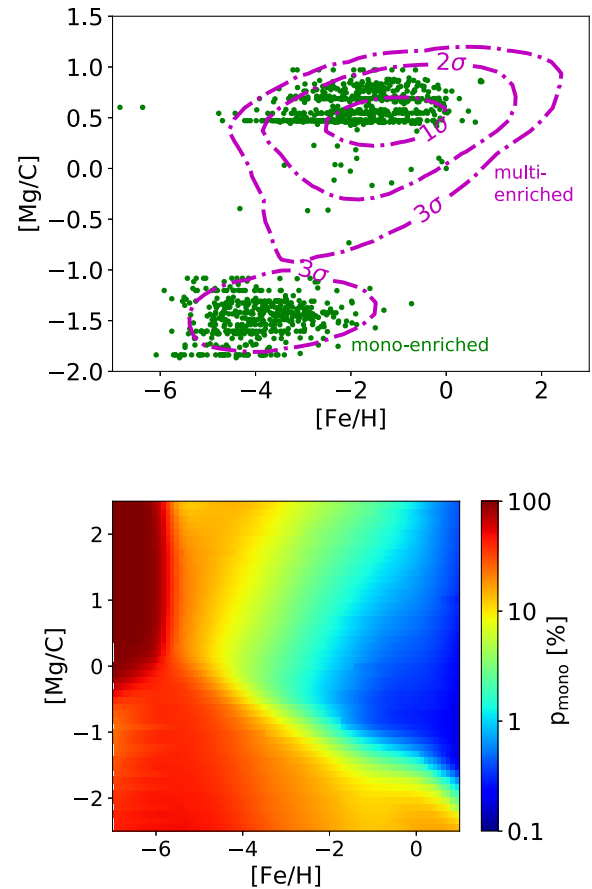


Figure 11. Top: Mono-enriched second-generation stars populate specific regions in this plot (green), compared to the distribution of multi-enriched second-generation stars, illustrated by the purple probability contours. Mono-enriched stars can be found at all metallicities up to almost solar, although most have $[\text{Fe}/\text{H}] < -2$, and so the metallicity alone is not a reliable diagnostic for whether the star is mono-enriched or multi-enriched. $[\text{Mg}/\text{C}]$ further helps to quantify the likelihood of the gas being enriched only once. Bottom: Probability of mono-enrichment, $p = N_{\text{mono}}/(N_{\text{multi}} + N_{\text{mono}})$, for the same elemental ratios as in the top panel. There are regions of the parameter space in our model with a probability of almost 100 per cent for finding second-generation stars that formed from gas that was enriched by only one previous SN. However, this probability does not reflect how many stars in total are expected in these regions, as we can see by comparing the two panels.

lower panel extends to regions that are not sampled in the top panel. The two events at $[\text{Fe}/\text{H}] < -6$ and $[\text{Mg}/\text{C}] \sim 0.6$ correspond to a very small hydrogen dilution mass and a star in this region would have a probability close to 100 per cent to be mono-enriched (see lower panel). However, there are no observed stars in this abundance regime yet (Suda et al. 2008; Abohalima & Frebel 2017).

4.2 The divergence of the chemical displacement

In this section, we propose a new, alternative method to identify mono-enriched EMP stars based on their chemical composition. This method is independent of the star formation model, computationally efficient, and the qualitative results are insensitive to assumptions about the IMF or the fraction of faint SNe. We first introduce the underlying analytical arguments of this new diagnostic, compare it to the results from our cosmological model, and finally apply it to observed EMP stars.

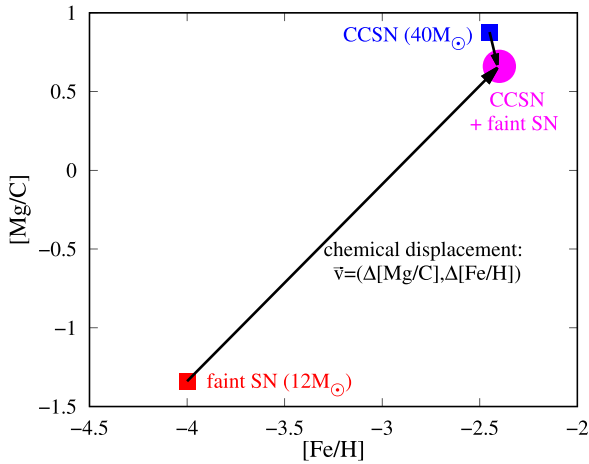


Figure 12. Illustration and definition of the chemical displacement for two example SNe. Combining the yields of two SNe with different progenitor masses results in an effective displacement of the ISM metal abundances. We define the chemical displacement as the resulting vector field of this operation.

4.2.1 Motivation and definition

Our new diagnostic is based on the chemical displacement, which is illustrated in Fig. 12. Commonly, the elemental abundances of observed EMP stars are plotted, but now we directly illustrate the SN yields and analyse how the chemical composition changes when we add the metal yields of two or more SNe. Each possible combination of SNe yields defines two vectors which point to the resulting ISM abundance, as illustrated by the two arrows in this example. The resulting vector field of the successive mixing of SN yields from different progenitor stars defines the chemical displacement, which we show in Fig. 13. This vector field of the chemical displacement reflects changes in the abundances ratios when more than one SN contributes to the metal enrichment. The local magnitude of this vector field quantifies the tendency for enriched gas to be displaced from this region (i.e. to change its [Mg/C] and [Fe/H] abundances) when the elements of an additional SN are added.

To further quantify the chemical displacement, and the most promising elements for identifying mono-enriched second-generation stars, we calculate the divergence of the chemical displacement field. The divergence describes the effective outward flux of a vector field that is emanating from a point. To guarantee numerical stability, we do not differentiate the resulting sparsely sampled vector field but apply Gauss’ theorem: for each point where a displacement vector starts, we add the length of this vector to the divergence of this point. Where a displacement vector ends, we subtract the length of this vector from the divergence of this point.

Regions in abundance space with a high negative divergence attract SN yield contributions from other regions of the abundance space. Conversely, areas with a high positive divergence represent regions for which mixing with the yields of a second SN shifts the elemental abundances out of this region.

The information about the exact enrichment channel cannot be reconstructed uniquely for stars in areas with a negative divergence. Therefore, the divergence of the chemical displacement simultaneously quantifies the information loss that occurs when combining several SN yields. A negative divergence corresponds to a high degeneracy.

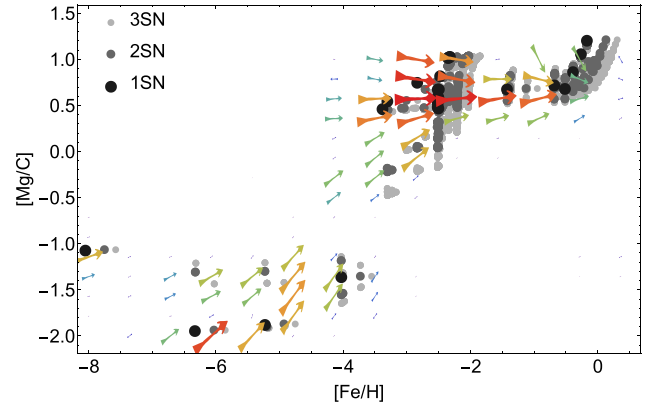


Figure 13. Illustration of the chemical displacement vector field of [Mg/C] and [Fe/H] for 25 SN progenitor masses, according to our fiducial IMF. The black points indicate the yields of single SNe for different progenitor masses. The 25^2 dark grey points indicate the abundance ratios produced by combining the elemental yields of all possible combinations of two SNe from our set of 25. Similarly, the 25^3 light grey points represent the combined yields of three Pop III SNe. This plot illustrates how adding yields from several SNe changes the typically expected elemental ratios. For hydrogen, we assume a constant dilution mass of $7 \times 10^5 M_{\odot}$, which is the median hydrogen mass in our sample of haloes that are about to form second-generation stars. The actual hydrogen mass and hence [Fe/H] might vary, but such an offset will not change the qualitative results for [Mg/C]. The length of the vectors illustrates the local magnitude of the chemical displacement field. The dynamical range of the vectors is decreased for better illustration and their length is therefore not to scale. The colour of the arrows is an additional qualitative guidance to illustrate the magnitude of the vector field.

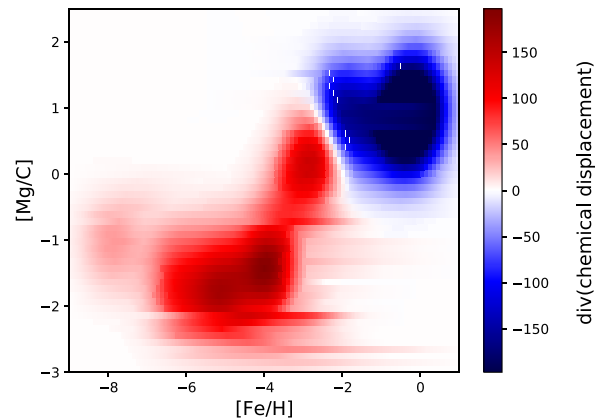


Figure 14. Divergence of the chemical displacement, based on the SN yields by Nomoto et al. (2013). Positive values indicate promising regions to find mono-enriched second-generation stars. Negative values represent attracting regions with a high chance of degeneracy due to yields being higher overall. To find mono-enriched second-generation stars, EMP stars with $[Mg/C] < -0.5$ should be selected. Stars with $[Mg/C] \sim 1$ and $[Fe/H] \gtrsim -3$ are likely to be enriched by multiple SNe.

4.2.2 Comparison to semi-analytical model

To highlight the strengths and weaknesses of our new diagnostic, we compare it to the probabilities of a star being mono-enriched, as derived from our cosmological model.

The divergence map for [Mg/C] can be seen in Fig. 14. This divergence map should be compared to Fig. 11 to see that we can reproduce the same trend with a more flexible method, fewer as-

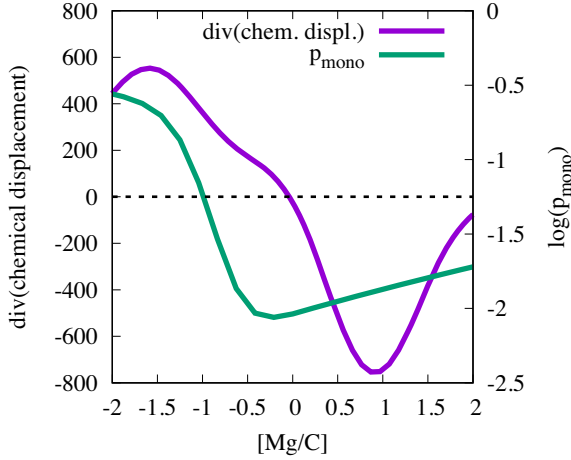


Figure 15. Comparison of the divergence of the chemical displacement (purple, left y-axis) to the probability of being mono-enriched based on our cosmological model (green, right y-axis). Due to the different units, the two methods can only be compared at a qualitative level. The overall behaviour and predictive power of the two diagnostics is generally the same: the maximum of the divergence of the chemical displacements corresponds to $p_{\text{mono}} \gtrsim 30$ per cent and a negative divergence to $p_{\text{mono}} \lesssim 3$ per cent.

assumptions regarding the details of Pop III star formation, and with less computational time. Our new diagnostic does not reproduce the high probability region at $[\text{Mg}/\text{C}] \gtrsim 0.5$ and $[\text{Fe}/\text{H}] < -5$ in the lower panel of Fig. 11 because this high probability of mono-enrichment emerges from only two events with a very small hydrogen dilution mass. The hydrogen dilution mass is assumed to be constant in our calculation of the chemical displacement.

The figure also highlights the dominating nature of core collapse ($[\text{Fe}/\text{H}] \sim -2$) and pair-instability SNe ($[\text{Fe}/\text{H}] \sim -1$), both around $0.5 < [\text{Mg}/\text{C}] < 1.0$. These SNe have high yields of Mg, C, and Fe and therefore dominate the metal mass budget over those of other SNe, after they were combined with the metal yields of a second or third SNe. This illustrates that it is generally difficult with our diagnostic to uniquely identify mono-enriched second-generation stars that have abundance ratios close to those produced by an SN with a high mass of ejected metals.

This implies an important consequence for EMP stars that formed from the gas enriched by such a dominating Pop III progenitor. Since the dominating Pop III SN has large absolute metal yields, it can thus not be excluded that another progenitor SNe with a lower yield is ‘hidden’ in the observed stellar signature. We thus conclude that only EMP stars enriched by one (faint) SN with a small absolute metal yield can be clearly identified as mono-enriched stars.

A direct comparison for $[\text{Mg}/\text{C}]$ in one dimension is given in Fig. 15. The different units of the two diagnostics allows only a qualitative comparison. Both methods identify the range below $[\text{Mg}/\text{C}] \lesssim -1$ as a promising region to find mono-enriched second-generation stars. The peak value of the divergence of the chemical displacements corresponds to probabilities around 30 per cent for finding mono-enriched stars using the results from our semi-analytical model. Conversely, a negative divergence of the chemical displacement at $[\text{Mg}/\text{C}] > 0$ corresponds to probabilities of $\lesssim 3$ per cent for mono-enrichment. This indicates an attracting region with a high degeneracy between mono- and multi-enriched second-generation stars.

This comparison shows a qualitative agreement between our semi-analytical cosmological model and the new diagnostic based

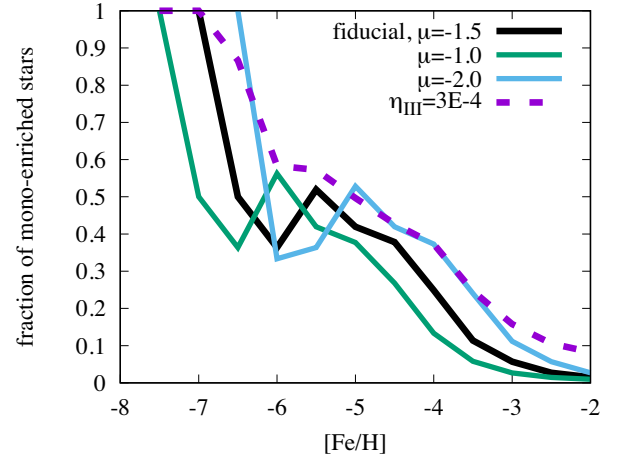


Figure 16. Fraction of mono-enriched second-generation stars as a function of the metallicity, based on our semi-analytical model. In our fiducial model, this fraction is 100 per cent for $[\text{Fe}/\text{H}] \lesssim -7$ and around 40 per cent in the range $-6 \lesssim [\text{Fe}/\text{H}] \lesssim -4$. There can also be multi-enriched second-generation stars at $[\text{Fe}/\text{H}] \lesssim -6$, although the probability for this case is small. This distribution depends on the SFE, η_{III} , and on the assumed fraction of hydrogen that mixes with the ejected metals after an enrichment event, 10^μ .

on the divergence of the chemical displacement. We highlight again that this new diagnostic is cheaper, more flexible and involves fewer free parameters than the full cosmological model.

4.2.3 Divergence in 1D

In the previously presented example, this diagnostic tool was derived in 2D for two elemental abundance ratios but it can also be applied in higher-dimensional vector spaces if information is available on additional abundance ratios or for a single elemental ratio to obtain the trends with these elements.

We canonically expect to find mono-enriched second-generation stars at the lowest metallicities (Ryan, Norris & Beers 1996), as we show in Fig. 16. This distribution is affected by the Pop III SFE and by the efficiency of metal mixing. Allowing the ejected metals to mix on average with a larger fraction of the gas in a halo ($\mu = -1.0$) shifts, this distribution to lower metallicities compared to the fiducial model. A lower SFE yields higher values for the fraction of mono-enriched second-generation stars at all metallicities because we expect fewer Pop III SN to explode per halo. The fraction of mono-enriched stars increases with decreasing metallicity. Therefore, the $[\text{Fe}/\text{H}]$ values on the abscissae of Figs 11–14 do not represent novel information as such.

In a further step, we therefore calculate the 1D divergence of various elemental ratios as an additional diagnostic. The results are shown in Fig. 17. This not only highlights the most promising abundance ratios that should be used to find mono-enriched second-generation stars, but it also allows us to compare different element diagnostics: the absolute value of the divergence quantifies how strongly a certain region is going to be attracting or repulsing. Moreover, it is important to examine the size of the difference in the abundance ratios between regions of positive and negative divergence. If this difference is too small, as for $[\text{Al}/\text{Mg}]$, uncertainties in both the aluminium and magnesium yields weaken the predictive power. A reliable diagnostic requires a peak of high divergence that is significantly separated from regions with negative divergence.

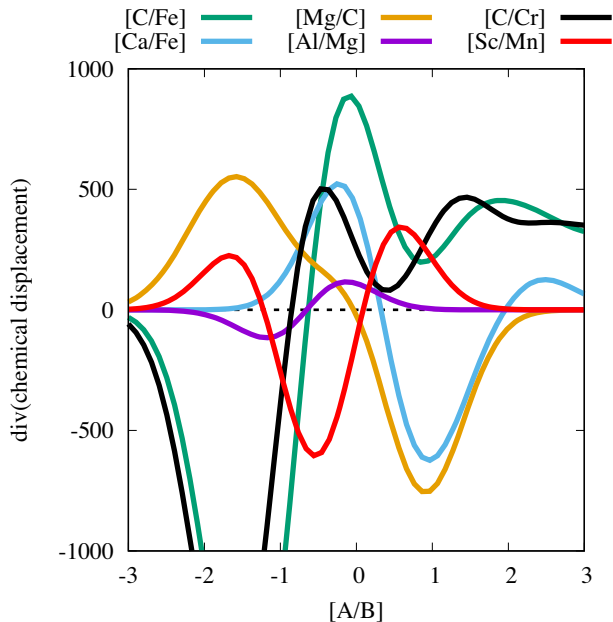


Figure 17. Divergence of the chemical displacement for various elemental abundance ratios. For example, $[\text{Mg}/\text{C}] < -0$ and $[\text{C}/\text{Fe}] \gtrsim 0$ are promising diagnostics to find mono-enriched second-generation stars. In contrast, $[\text{Al}/\text{Mg}]$ cannot be used because the overall range of possible elemental ratios (<1 dex) is of the same order as errors in the model and abundance estimates.

Although $[\text{C}/\text{Fe}] \sim -0.2$ seems to be a promising value to find mono-enriched stars, we note that this abundance range not only reflects the typical yield of Pop III core-collapse SNe but also corresponds to the yield from core-collapse SNe that arise from Pop I metal-rich stars. This immediately illustrates the limitations of our diagnostic tool, as it does not include the yields of all possible metal sources self-consistently.

4.2.4 Applying the new diagnostic to EMP stars

We apply our new diagnostic to a selection of observed stars from the JINAbase (Abotalima & Frebel 2017). We select all stars with $[\text{Fe}/\text{H}] < -4.5$ and chose the elements for which this sample is most complete (see Fig. 18).

We will provide a more detailed comparison to observations in a follow-up study but already briefly summarize the main conclusions and shortcomings here. Most of these EMP stars have a positive divergence of the chemical displacement and are therefore likely to be mono-enriched. The $[\text{N}/\text{Na}]$ ratio of at least three stars, however, corresponds to a negative divergence: DC-38245 (Cayrel et al. 2004), CS30336-049 (Yong et al. 2013), and HE 1327-2326 (Frebel et al. 2008). Some other stars with only upper limits are in the same region of negative divergence, which could be interpreted as a signature for multi-enrichment. The yields of nitrogen and sodium are sensitive to stellar rotation, which is not included in the models by Nomoto et al. (2013), and their abundance is difficult to derive accurately due to artificial nitrogen enhancement through the CNO cycle. Also differences between 1D and 3D non-local thermodynamic equilibrium stellar atmosphere models can affect the abundance by more than 0.5 dex.

Some observed EMP stars are outside the boundaries of our model, i.e. in regions for which we do not predict a value of the divergence. This is due to our limited sample of elemental yields,

which for example does not include hypernovae or mass transfer from an asymptotic giant branch star across a binary system as possible sources of metals. Moreover, we only assume SN models with one explosion energy per progenitor mass and no rotation of the progenitor star. These effects would increase the diversity of possible elemental ratios and therefore widen the parameter space for which we can calculate the divergence of the chemical displacement. In a future study, we will improve this diagnostic, by taking into account a larger variety of sources for metals in the early Universe.

5 DISCUSSION

Our novel diagnostic based on the divergence of the chemical displacement can be applied to assess the likelihood of a star to be mono-enriched. A representation of the divergence such as in Fig. 17 or 18 will be most useful to classify metal-poor stars based on their measured abundances. However, the divergence of the chemical displacement cannot be directly translated into a probability of mono-enrichment. It rather reveals regions with a positive divergence in the multidimensional space of stellar abundances, which are dominantly populated by mono-enriched stars. A negative divergence is not a sufficient condition for multi-enrichment. A mono-enriched star can also be found in regions with a negative divergence, if it formed from gas enriched by an SN with high-metal yields. In a future project, we will improve this diagnostic and apply it to further EMP stars.

Ji et al. (2015) also considered how the abundance of second-generation stars would be affected by forming a small multiple of Pop III stars in minihaloes. They focused on two specific scenarios of second-generation star formation: immediate gas recollapse in a minihalo and delayed formation in atomic cooling haloes. These cases are applicable in the earliest stages of Pop III and Pop II star formation, but at later times global radiative feedback becomes important. Our model includes the effect of external radiation in a cosmological context, extending its applicability to lower redshifts. Ji et al. (2015) also focused on specific element ratios with critical ratios to investigate the carbon-enhanced and pair instability SN signatures. Our new chemical divergence formalism generalizes their approach and allows more efficient searching of the ideal ratios in the full abundance space, independent of the specific assumptions of star formation.

5.1 Which element traces the total metal content best?

In theoretical models of cosmic chemical evolution or of the formation of the first low-mass stars, the total metal content is of fundamental importance. The metal content of a star is defined as the relative abundance of all elements heavier than helium, relative to our Sun, which consists of ~ 2 per cent metals: $Z/Z_{\odot} = \log_{10}(M_{\text{metals}}/(0.02M_{\text{gas}}))$. To connect this total metallicity to the observed abundances of individual elements, we show in Fig. 19 which element is a reliable tracer for the total metal content of a star.

We find that $[\text{Ca}/\text{H}]$ is on average about 1 dex above Z/Z_{\odot} for second-generation stars, albeit with a large scatter. Iron and carbon abundances are more reliable tracers for the total metal content of a star and the usage of calcium can lead to severe misinterpretations: stars with an estimated $[\text{Ca}/\text{H}] \approx -2$ may have an overall metallicity of $Z/Z_{\odot} < -3$ and therefore be falsely rejected for any spectroscopic follow-up study. These results are a consequence of our assumed SN yields, which also show an IMF-averaged offset

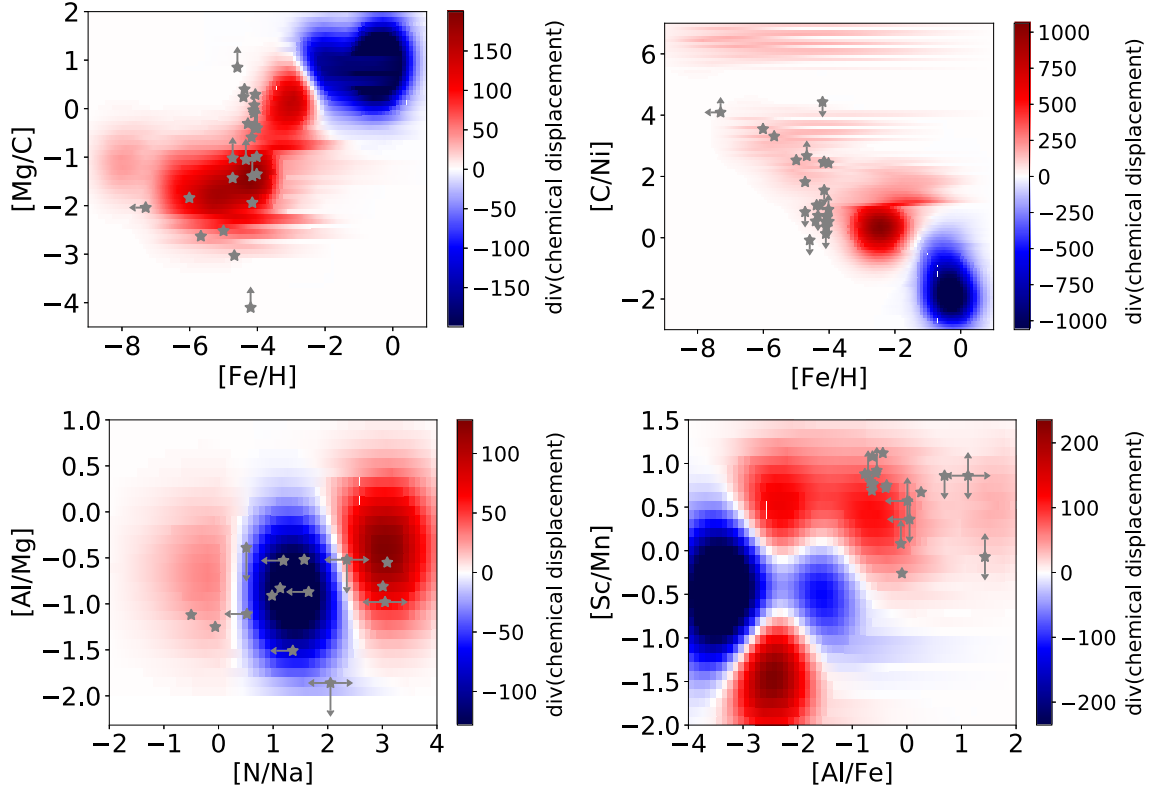


Figure 18. Maps of the divergence of the chemical displacement for different elemental ratios overplotted with a sample of EMP stars from the JINAbase (Abohalima & Frebel 2017). Upper limits on the measured abundances are illustrated as arrows. This representation allows us to infer the trends of the stars being mono- or multi-enriched. Stars in regions with a high positive divergence (red) are likely to be mono-enriched, whereas a high negative divergence (blue) indicates a possible degeneracy of elemental yields and therefore a high probability of being multi-enriched. These divergence maps are based on the SN yields by Nomoto et al. (2013).

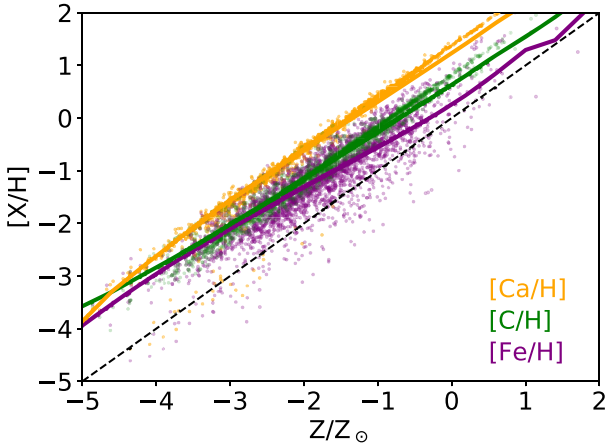


Figure 19. Individual elemental abundances as a function of the total metal content of second-generation stars in our model. The three coloured lines indicate the binned medians of these distributions. Iron and carbon are better tracers of the total metallicity of second-generation stars than calcium. Whereas the $[\text{Fe}/\text{H}]$ distribution lies closer to the diagonal (black dashed) and that for $[\text{C}/\text{H}]$ slightly above, the mostly likely value for $[\text{Ca}/\text{H}]$ is 1 dex above the corresponding Z/Z_{\odot} . For better illustration, we only plot a small subset of all second-generation stars.

of ~ 0.5 dex for $[\text{Ca}/\text{C}]$ and $[\text{Ca}/\text{Fe}]$. We also find the inverse possibility, mostly for calcium and iron, that a star with a low individual abundance of these elements can still have a high total metal content

(below dashed diagonal). These results are insensitive to the treatment of hydrogen dilution because all derived ratios scale equally with the hydrogen mass.

We further quantify the scatter of the distributions and find that carbon at $Z/Z_{\odot} < -3$ has the smallest standard deviation of ~ 1 dex and both calcium and iron have a scatter of ~ 1.2 dex in the same range of the overall stellar metal content.

The commonly used pre-selection method is to identify EMP candidates based on the Ca K line (see e.g. Keller et al. 2007; Koch et al. 2016; Starkenburg et al. 2017b) because it is strong, easy to see in low-quality data, and therefore most efficient regarding telescope time. Metal-poor stars show weaker calcium absorption features than more metal-rich stars. The additional use of a carbon-sensitive filter (e.g. the G-band around $\sim 4300 \text{ \AA}$) could yield a more reliable photometric estimate for the total metal content, although this suggestion has to be treated with caution when explicitly targeting CEMP stars.

We further analyse the fraction of EMP stars that a survey misses due to a too conservative calcium-based pre-selection. In Fig. 20, we show an example model for the fraction of falsely rejected stars.

If we are interested in EMP stars with $[\text{Fe}/\text{H}] < -3$ and assume that calcium traces iron with $[\text{Ca}/\text{H}] = [\text{Fe}/\text{H}] + 0.2$, a survey would reject stars with $[\text{Ca}/\text{H}] > -2.8$ as too metal rich. However, in the range

$$-2.8 < [\text{Ca}/\text{H}] < -2.0 \quad (11)$$

we find 12 per cent of second-generation stars with $[\text{Fe}/\text{H}] < -3$. In particular, PISNe with a progenitor mass around $\sim 150 M_{\odot}$ eject

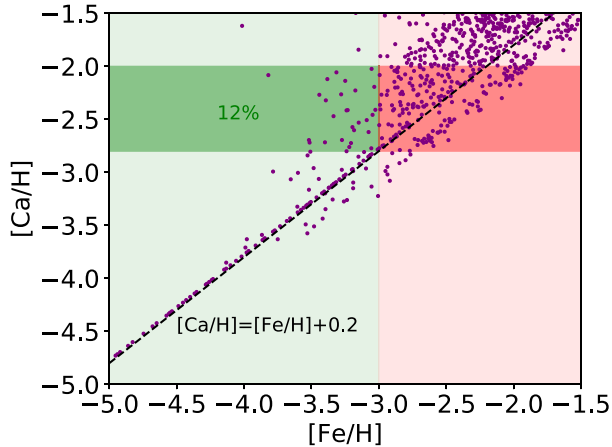


Figure 20. Calcium against iron abundance for second-generation stars. The dark region represents the fraction of EMP stars ($[\text{Fe}/\text{H}] < -3$) that a survey would miss if it only selects stars with $[\text{Ca}/\text{H}] < -2.8$ instead of $[\text{Ca}/\text{H}] < -2.0$ for a higher resolution follow-up observation.

material with high $[\text{Ca}/\text{Fe}]$ yields (Karlsson, Johnson & Bromm 2008) and so second-generation stars enriched primarily by these PISNe will have high $[\text{Ca}/\text{Fe}]$. Our estimate can be used as an approximation for the completeness of surveys, although we note that our simulated sample might not be complete in this calcium range since we do not include enrichment by later generations of star formation. For an assumed relation of $[\text{Ca}/\text{H}] = [\text{Fe}/\text{H}] + 0.4$, we still find ~ 11 per cent of EMP stars in the corresponding range

$$-2.6 < [\text{Ca}/\text{H}] < -2.0. \quad (12)$$

5.2 Caveats

Our diagnostic and predictions based on the divergence of the chemical displacement are only as good as the underlying models for the SN nucleosynthetic yields. We use the tabulated SN yields as a function of the Pop III progenitor mass by Nomoto et al. (2013) with additional models for faint SNe by Ishigaki et al. (2014). In a future study, we will improve our model by including the metal contributions from other enrichment channels, such as neutron star mergers, hypernovae, AGB stars, and Type Ia SNe. Moreover, we will assess the sensitivity of our model to the assumed Pop III SN yield models and derive a diagnostic based on elements that are least sensitive to the underlying model assumptions.

We include Pop III star formation as a sub-grid model based on the random sampling of individual stars from a given IMF. However, UV feedback by the primary formed massive star in a minihalo might prevent the formation of further massive stars (Susa et al. 2014; Hosokawa et al. 2016). Such a suppression of further Pop III stars with higher masses might result in a steeper slope of the IMF at higher masses. Moreover, we have no information on the exact position of the first stars in a minihalo. Therefore, we cannot take into account the effect of SNe that explode off-centre in the halo and have different metal ejection fractions, mixing efficiencies, or recovery times for the ISM.

Throughout the paper, we do not track individual second-generation stars. We rather follow their formation events and assume that such a burst of star formation creates a chemically homogeneous population of second-generation stars. Therefore we cannot make reliable predictions about the absolute number of second-generation stars in our model. Moreover, the number of stars per halo might

differ depending on the environment and the available gas mass. Larger systems, which are more likely to experience multiple previous SNe, will also host more second-generation stars. This is an additional bias that reduces the relative number of mono-enriched second-generation stars, which tend to form in less massive systems.

6 SUMMARY AND CONCLUSION

EMP stars in the MW provide a unique way to probe the mass distribution of the first stars. They carry the characteristic chemical fingerprint of the SN that enriched the gas from which they formed. A comparison of their observed chemical abundances with models of Pop III SNe allows us to determine the Pop III progenitor masses of the SNe. To fully exploit this method and avoid degeneracies in the fitting of the SN yields, it has to be applied to mono-enriched second-generation stars.

In this paper, we have presented a novel diagnostic to identify this precious subclass of mono-enriched stars. We model the first generations of star formation with a semi-analytical model, based on dark matter merger trees from the Caterpillar simulations (Griffen et al. 2016). We find that the Pop III SFE, the primordial IMF, the mixing efficiency of metals with the ISM, and the fraction of faint SNe are the main parameters to calibrate our model. The MDF and fraction of CEMP stars as observational constraints are best reproduced by our fiducial model with a logarithmically flat IMF in the mass range of $3\text{--}150 M_{\odot}$. With a two-sample KS test, we can exclude a Pop III IMF that extends up to $M_{\text{max}} = 300 M_{\odot}$ at the 95 per cent level. In our model, PISNe from stars with masses of $\gtrsim 200 M_{\odot}$ fail to reproduce the MDF at $[\text{Fe}/\text{H}] \leq -3$ due to their high absolute metal yields.

Mono-enriched stars account for only ~ 1 per cent of second-generation stars in our fiducial model. This fraction is a strong function of the primordial SFE, and we provide an analytical formula to independently calculate this fraction for different model assumptions (equation 10). Dwarf satellites have the highest stellar fraction of mono-enriched second-generation stars because they formed the majority of their stellar population early on. Satellites with $M_h < 10^9 M_{\odot}$ host 10–100 per cent second-generation stars and satellites with $M_h \lesssim 10^8 M_{\odot}$ contain only second-generation stars, some of them only mono-enriched second-generation stars. The specific numbers have to be treated with caution, since they are affected by uncertainties in the abundance matching.

We have also presented a novel analytical diagnostic to identify mono-enriched stars, based on the divergence of the chemical displacement. This new diagnostic allows to derive the likelihood of mono-enrichment independently from most parameters that govern the first billion years. The fraction of mono-enriched second-generation stars is 100 per cent for $[\text{Fe}/\text{H}] \leq -7$ and around 40 per cent in the range $-6 \lesssim [\text{Fe}/\text{H}] \lesssim -4$. We also present additional elemental ratios that are reliable tracers for mono-enrichment, such as $[\text{Mg}/\text{C}] < -1$, $[\text{Sc}/\text{Mn}] < 0.5$, $[\text{C}/\text{Cr}] > 0.5$, or $[\text{Ca}/\text{Fe}] > 2$.

The chemical imprint of SNe with little ejected metals could be hidden in the abundance patterns from stars with more metals and consequently only faint SNe can be uniquely identified as being mono-enriched. Thus, focusing on mono-enriched stars biases the interpretation towards Pop III progenitors with low metal yields. A negative divergence of the chemical displacement does not mean that such a star is multi-enriched, but that there is a certain possibility that this abundance pattern is the result of multi-enrichment.

The results of our study provide powerful diagnostic to interpret extensive photometric and spectroscopic data of metal-poor stars in

the MW and its satellites, which will be available in the next decades. Specifically, our findings can be applied to data from narrow-band photometric surveys covering the Ca H&K feature, such as the Pristine survey (Starkenburg et al. 2017b), which provide unbiased view of the most metal-poor stars up to a large Galactic distance. Next-generation low and medium-resolution spectroscopic facilities such as WEAVE (Bonifacio et al. 2016) or PFS (Takada et al. 2014) are suitable for directly identifying mono-enriched second-generation stars among MW field halo and dwarf satellite's stars, which will be the best targets for a follow-up high-resolution spectroscopy. High-resolution spectroscopic surveys for large samples of stars in the MW are also ongoing or planned in the near future with high-resolution multi-object spectrographs such as the APOGEE (Majewski et al. 2017), GALAH (De Silva et al. 2015), and the 4MOST (Feltzing et al. 2017) projects.

ACKNOWLEDGEMENTS

We thank the reviewer for constructive suggestions and careful reading of the manuscript. The authors would like to thank Ken'ichi Nomoto, Gen Chiaki, Hajime Susa, Kazu Omukai, and Wako Aoki for valuable discussions and helpful contributions. TH is a JSPS International Research Fellow. The authors were supported by the European Research Council under the European Community's Seventh Framework Programme (FP7/2007-2013) via the ERC Advanced Grant 'STARLIGHT: Formation of the First Stars' under the project number 339177 (RSK) and via the ERC Grant 'BLACK' under the project number 614199 (TH). SCOG and RSK also acknowledge funding from the Deutsche Forschungsgemeinschaft via SFB 881 'The Milky Way System' (subprojects B1, B2, and B8) and SPP 1573 'Physics of the Interstellar Medium' (grant numbers KL 1358/18.1, KL 1358/19.2, and GL 668/2-1). AF is supported by NSF CAREER grant AST-1255160. This research has been supported by the Canon Research Foundation. This research is further supported in part by the National Science Foundation (NSF; USA) under grant no. PHY-1430152 (JINA Center for the Evolution of the Elements). APJ is supported by NASA through Hubble Fellowship grant HST-HF2-51393.001 awarded by the Space Telescope Science Institute, which is operated by the Association of Universities for Research in Astronomy, Inc., for NASA, under contract NAS5-26555. BWO was supported by the National Aeronautics and Space Administration (NASA) through grant NNX15AP39G and Hubble Theory Grant HST-AR-13261.01-A, and by the NSF through grant AST-1514700. Computational support for the Caterpillar simulations was provided by XSEDE through the grant nos TG-AST120022 and TG-AST110038. Computations were carried out on the compute cluster of the Astrophysics Division which was built with support from the Kavli Investment Fund, administered by the MIT Kavli Institute for Astrophysics and Space Research. This work was supported by World Premier International Research Center Initiative (WPI Initiative), MEXT, Japan.

REFERENCES

Abohalima A., Frebel A., 2017, pr eprint ([arXiv:1711.04410](https://arxiv.org/abs/1711.04410))
 Aoki W., Beers T. C., Christlieb N., Norris J. E., Ryan S. G., Tsangarides S., 2007, *ApJ*, 655, 492
 Aoki W., Tominaga N., Beers T. C., Honda S., Lee Y. S., 2014, *Science*, 345, 912
 Asplund M., Grevesse N., Sauval A. J., Scott P., 2009, *ARA&A*, 47, 481
 Barkat Z., Rakavy G., Sack N., 1967, *Phys. Rev. Lett.*, 18, 379
 Beers T. C., Preston G. W., Shtetman S. A., 1992, *AJ*, 103, 1987

Bond H. E., 1981, *ApJ*, 248, 606
 Bond J. R., Arnett W. D., Carr B. J., 1984, *ApJ*, 280, 825
 Bonifacio P. et al., 2015, *A&A*, 579, A28
 Bonifacio P. et al., Paris, French Society of Astronomy and Astrophysics, 2016, in Reylé C., Richard J., Cambrésy L., Deleuil M., Pécontal E., Tresse L., Vauglin I., eds, SF2A-2016: Proceedings of the Annual meeting of the French Society of Astronomy and Astrophysics. p. 267
 Bower R. G., Vernon I., Goldstein M., Benson A. J., Lacey C. G., Baugh C. M., Cole S., Frenk C. S., 2010, *MNRAS*, 407, 2017
 Bullock J. S., Kravtsov A. V., Weinberg D. H., 2000, *ApJ*, 539, 517
 Caffau E. et al., 2016, *A&A*, 595, L6
 Cayrel R. et al., 2004, *A&A*, 416, 1117
 Chen K.-J., Heger A., Whalen D. J., Moriya T. J., Bromm V., Woosley S. E., 2017a, *MNRAS*, 467, 4731
 Chen K.-J., Whalen D. J., Wollenberg K. M. J., Glover S. C. O., Klessen R. S., 2017b, *ApJ*, 844, 111
 Chiaki G., Yoshida N., Hirano S., 2016, *MNRAS*, 463, 2781
 Chiaki G., Susa H., Hirano S., 2018, *MNRAS*, 475, 4378
 Clark P. C., Glover S. C. O., Smith R. J., Greif T. H., Klessen R. S., Bromm V., 2011, *Science*, 331, 1040
 Cohen J. G., Christlieb N., Thompson I., McWilliam A., Shtetman S., Reimers D., Wisotzki L., Kirby E., 2013, *ApJ*, 778, 56
 Cooke R. J., Madau P., 2014, *ApJ*, 791, 116
 Cooke R., Pettini M., Steidel C. C., Rudie G. C., Jorgenson R. A., 2011, *MNRAS*, 412, 1047
 de Bennassuti M., Salvadori S., Schneider R., Valiante R., Omukai K., 2017, *MNRAS*, 465, 926
 De Silva G. M. et al., 2015, *MNRAS*, 449, 2604
 Dijkstra M., Haiman Z., Mesinger A., Wyithe J. S. B., 2008, *MNRAS*, 391, 1961
 Drlica-Wagner A. et al., 2015, *ApJ*, 813, 109
 Dutta J., Sur S., Stacy A., Singh Bagla J., 2017, pr eprint ([arXiv:1712.06912](https://arxiv.org/abs/1712.06912))
 Feltzing S. et al., 2017, preprint ([arXiv:1708.08884](https://arxiv.org/abs/1708.08884))
 Fraley G. S., 1968, *Ap&SS*, 2, 96
 Fraser M., Casey A. R., Gilmore G., Heger A., Chan C., 2017, *MNRAS*, 468, 418
 Frebel A., Norris J. E., 2015, *ARA&A*, 53, 631
 Frebel A., Norris J. E., Aoki W., Honda S., Bessell M. S., Takada-Hidai M., Beers T. C., Christlieb N., 2007, *ApJ*, 658, 534
 Frebel A., Collet R., Eriksson K., Christlieb N., Aoki W., 2008, *ApJ*, 684, 588
 Frebel A., Johnson J. L., Bromm V., 2009, *MNRAS*, 392, L50
 Fryer C. L., Woosley S. E., Heger A., 2001, *ApJ*, 550, 372
 Gao L., Theuns T., Frenk C. S., Jenkins A., Helly J. C., Navarro J., Springel V., White S. D. M., 2010, *MNRAS*, 403, 1283
 Garrison-Kimmel S., Boylan-Kolchin M., Bullock J. S., Lee K., 2014, *MNRAS*, 438, 2578
 Garrison-Kimmel S., Bullock J. S., Boylan-Kolchin M., Bardwell E., 2017, *MNRAS*, 464, 3108
 Glover S., 2013, in Wiklind T., Mobasher B., Bromm V., eds, *Astrophysics and Space Science Library*, Vol. 396, *The First Galaxies, The First Galaxies*. Springer-Verlag, Berlin, p. 103
 Gómez F. A., Coleman-Smith C. E., O'Shea B. W., Tumlinson J., Wolpert R. L., 2012, *ApJ*, 760, 112
 Gómez F. A., Coleman-Smith C. E., O'Shea B. W., Tumlinson J., Wolpert R. L., 2014, *ApJ*, 787, 20
 Greif T. H., 2015, *Comput. Astrophys. Cosmol.*, 2, 3
 Greif T. H., Bromm V., 2006, *MNRAS*, 373, 128
 Greif T. H., Johnson J. L., Bromm V., Klessen R. S., 2007, *ApJ*, 670, 1
 Greif T. H., Glover S. C. O., Bromm V., Klessen R. S., 2010, *ApJ*, 716, 510
 Greif T. H., White S. D. M., Klessen R. S., Springel V., 2011a, *ApJ*, 736, 147
 Greif T. H., Springel V., White S. D. M., Glover S. C. O., Clark P. C., Smith R. J., Klessen R. S., Bromm V., 2011b, *ApJ*, 737, 75
 Griffen B. F., Ji A. P., Dooley G. A., Gómez F. A., Vogelsberger M., O'Shea B. W., Frebel A., 2016, *ApJ*, 818, 10
 Griffen B. F., Dooley G. A., Ji A. P., O'Shea B. W., Gómez F. A., Frebel A., 2018, *MNRAS*, 474, 443

- Hartwig T., Bromm V., Klessen R. S., Glover S. C. O., 2015, *MNRAS*, 447, 3892
- Hattori K., Yoshii Y., Beers T. C., Carollo D., Lee Y. S., 2014, *ApJ*, 784, 153
- Heger A., Woosley S. E., 2002, *ApJ*, 567, 532
- Heger A., Woosley S. E., 2010, *ApJ*, 724, 341
- Hirai Y., Saitoh T. R., 2017, *ApJ*, 838, L23
- Hirano S., Bromm V., 2017, *MNRAS*, 470, 898
- Hirano S., Hosokawa T., Yoshida N., Umeda H., Omukai K., Chiaki G., Yorke H. W., 2014, *ApJ*, 781, 60
- Hirano S., Hosokawa T., Yoshida N., Kuiper R., 2017, *Science*, 357, 1375
- Hosokawa T., Hirano S., Kuiper R., Yorke H. W., Omukai K., Yoshida N., 2016, *ApJ*, 824, 119
- Hummel J. A., Pawlik A. H., Milosavljević M., Bromm V., 2012, *ApJ*, 755, 72
- Ishigaki M. N., Tominaga N., Kobayashi C., Nomoto K., 2014, *ApJ*, 792, L32
- Ishigaki M. N., Tominaga N., Kobayashi C., Nomoto K., 2018, preprint (arXiv:1801.07763)
- Ishiyama T., Sudo K., Yokoi S., Hasegawa K., Tominaga N., Susa H., 2016, *ApJ*, 826, 9
- Jeon M., Pawlik A. H., Bromm V., Milosavljević M., 2014, *MNRAS*, 444, 3288
- Jeon M., Besla G., Bromm V., 2017, *ApJ*, 848, 85
- Ji A. P., Frebel A., Bromm V., 2015, *MNRAS*, 454, 659
- Ji A. P., Frebel A., Chiti A., Simon J. D., 2016, *Nature*, 531, 610
- Johnson J. L., 2015, *MNRAS*, 453, 2771
- Johnson J. L., Dalla Vecchia C., Khochfar S., 2013, *MNRAS*, 428, 1857
- Karlsson T., Johnson J. L., Bromm V., 2008, *ApJ*, 679, 6
- Kauffmann G., White S. D. M., Guiderdoni B., 1993, *MNRAS*, 264, 201
- Keller S. C. et al., 2007, *PASA*, 24, 1
- Keller S. C. et al., 2014, *Nature*, 506, 463
- Kim S. Y., Peter A. H. G., Hargis J. R., 2017, preprints (arXiv:1711.06267)
- Kirby E. N., Simon J. D., Geha M., Guhathakurta P., Frebel A., 2008, *ApJ*, 685, L43
- Kitayama T., Yoshida N., 2005, *ApJ*, 630, 675
- Klypin A., Kravtsov A. V., Valenzuela O., Prada F., 1999, *ApJ*, 522, 82
- Koch A., McWilliam A., Preston G. W., Thompson I. B., 2016, *A&A*, 587, A124
- Komiya Y., Shigeyama T., 2016, *ApJ*, 830, 76
- Komiya Y., Habe A., Suda T., Fujimoto M. Y., 2010, *ApJ*, 717, 542
- Komiya Y., Suda T., Fujimoto M. Y., 2015, *ApJ*, 808, L47
- Komiya Y., Suda T., Fujimoto M. Y., 2016, *ApJ*, 820, 59
- Lee Y. S. et al., 2013, *AJ*, 146, 132
- Limongi M., Chieffi A., 2012, *ApJS*, 199, 38
- Loeb A., 2010, *How Did the First Stars and Galaxies Form?* Princeton Univ. Press, Princeton, NJ
- Maeder A., Meynet G., Chiappini C., 2015, *A&A*, 576, A56
- Magg M., Hartwig T., Glover S. C. O., Klessen R. S., Whalen D. J., 2016, *MNRAS*, 462, 3591
- Magg M., Hartwig T., Agarwal B., Frebel A., Glover S. C. O., Griffen B. F., Klessen R. S., 2018, *MNRAS*, 473, 5308
- Majewski S. R. et al., 2017, *AJ*, 154, 94
- Moore B., Ghigna S., Governato F., Lake G., Quinn T., Stadel J., Tozzi P., 1999, *ApJ*, 524, L19
- Munshi F., Brooks A. M., Applebaum E., Weisz D. R., Governato F., Quinn T. R., 2017, preprint (arXiv:1705.06286)
- Naoz S., Yoshida N., Gnedin N. Y., 2013, *ApJ*, 763, 27
- Nomoto K., Kobayashi C., Tominaga N., 2013, *ARA&A*, 51, 457
- Norris J. E. et al., 2013, *ApJ*, 762, 28
- O'Shea B. W., Norman M. L., 2008, *ApJ*, 673, 14
- O'Shea B. W., Wise J. H., Xu H., Norman M. L., 2015, *ApJ*, 807, L12
- Placco V. M., Frebel A., Beers T. C., Stancliffe R. J., 2014, *ApJ*, 797, 21
- Placco V. M., Frebel A., Lee Y. S., Jacobson H. R., Beers T. C., Pena J. M., Chan C., Heger A., 2015, *ApJ*, 809, 136
- Placco V. M. et al., 2016, *ApJ*, 833, 21
- Planck Collaboration XVI, 2014, *A&A*, 571, A16
- Planck Collaboration XIII 2016, *A&A*, 594, A13
- Rakavy G., Shaviv G., 1967, *ApJ*, 148, 803
- Ritter J. S., Safrank-Shrader C., Gnat O., Milosavljević M., Bromm V., 2012, *ApJ*, 761, 56
- Ritter J. S., Sluder A., Safrank-Shrader C., Milosavljević M., Bromm V., 2015, *MNRAS*, 451, 1190
- Ritter J. S., Safrank-Shrader C., Milosavljević M., Bromm V., 2016, *MNRAS*, 463, 3354
- Roederer I. U., Preston G. W., Thompson I. B., Shtetman S. A., Sneden C., Burley G. S., Kelson D. D., 2014, *AJ*, 147, 136
- Ryan S. G., Norris J. E., Beers T. C., 1996, *ApJ*, 471, 254
- Safrank-Shrader C., Milosavljević M., Bromm V., 2014, *MNRAS*, 440, L76
- Salvadori S., Ferrara A., 2009, *MNRAS*, 395, L6
- Sarmento R., Scannapieco E., Pan L., 2017, *ApJ*, 834, 23
- Sarmento R., Scannapieco E., Cohen S., 2018, *ApJ*, 854, 75
- Schauer A. T. P., Whalen D. J., Glover S. C. O., Klessen R. S., 2015, *MNRAS*, 454, 2441
- Schauer A. T. P., Regan J., Glover S. C. O., Klessen R. S., 2017, *MNRAS*, 471, 4878
- Schörck T. et al., 2009, *A&A*, 507, 817
- Seitzzahl I. R. et al., 2013, *MNRAS*, 429, 1156
- Sharma M., Theuns T., Frenk C. S., Cooke R. J., 2018, *MNRAS*, 473, 984
- Shen S., Kulkarni G., Madau P., Mayer L., 2017, *MNRAS*, 469, 4012
- Skúladóttir Á., Tolstoy E., Salvadori S., Hill V., Pettini M., Shetrone M. D., Starkenburg E., 2015, *A&A*, 574, A129
- Smith R. J., Glover S. C. O., Clark P. C., Greif T., Klessen R. S., 2011, *MNRAS*, 414, 3633
- Smith B. D., Wise J. H., O'Shea B. W., Norman M. L., Khochfar S., 2015, *MNRAS*, 452, 2822
- Stacy A., Greif T. H., Bromm V., 2010, *MNRAS*, 403, 45
- Stacy A., Bromm V., Loeb A., 2011, *ApJ*, 730, L1
- Starkenburg E. et al., 2013, *MNRAS*, 429, 725
- Starkenburg E., Oman K. A., Navarro J. F., Crain R. A., Fattahi A., Frenk C. S., Sawala T., Schaye J., 2017a, *MNRAS*, 465, 2212
- Starkenburg E. et al., 2017b, *MNRAS*, 471, 2587
- Suda T. et al., 2008, *PASJ*, 60, 1159
- Susa H., Hasegawa K., Tominaga N., 2014, *ApJ*, 792, 32
- Takada M. et al., 2014, *PASJ*, 66, R1
- Tanaka T. L., Li M., 2014, *MNRAS*, 439, 1092
- Tanaka S. J., Chiaki G., Tominaga N., Susa H., 2017, *ApJ*, 844, 137
- Tominaga N., Umeda H., Nomoto K., 2007, *ApJ*, 660, 516
- Tominaga N., Iwamoto N., Nomoto K., 2014, *ApJ*, 785, 98
- Turk M. J., Abel T., O'Shea B., 2009, *Science*, 325, 601
- Vasiliev E. O., Vorobyov E. I., Matvienko E. E., Razoumov A. O., Shchekinov Y. A., 2012, *Astronomy Reports*, 56, 895
- Vincenzo F., Matteucci F., Belfiore F., Maiolino R., 2016, *MNRAS*, 455, 4183
- Visbal E., Haiman Z., Bryan G. L., 2015, *MNRAS*, 453, 4456
- Visbal E., Haiman Z., Bryan G. L., 2018, *MNRAS*, 475, 5246
- Weisz D. R., Dolphin A. E., Skillman E. D., Holtzman J., Gilbert K. M., Dalcanton J. J., Williams B. F., 2014, *ApJ*, 789, 147
- Whalen D., van Veelen B., O'Shea B. W., Norman M. L., 2008, *ApJ*, 682, 49
- Whalen D. J., Johnson J. L., Smidt J., Meiksin A., Heger A., Even W., Fryer C. L., 2013, *ApJ*, 774, 64
- Wise J. H., Abel T., 2008, *ApJ*, 685, 40
- Wise J. H., Turk M. J., Norman M. L., Abel T., 2012, *ApJ*, 745, 50
- Yong D. et al., 2013, *ApJ*, 762, 27
- Yoshida N., Abel T., Hernquist L., Sugiyama N., 2003, *ApJ*, 592, 645
- Yoshii Y., 1981, *A&A*, 97, 280

This paper has been typeset from a $\text{\TeX}/\text{\LaTeX}$ file prepared by the author.